NEUROSCIENCE

Efficient cortical coding of 3D posture in freely behaving rats

Bartul Mimica*†, Benjamin A. Dunn*, Tuce Tombaz,
V. P. T. N. C. Srikanth Bojja, Jonathan R. Whitlock†

Animals constantly update their body posture to meet behavioral demands, but little is known about the neural signals on which this depends. We therefore tracked freely foraging rats in three dimensions while recording from the posterior parietal cortex (PPC) and the frontal motor cortex (M2), areas critical for movement planning and navigation. Both regions showed strong tuning to posture of the head, neck, and back, but signals for movement were much less dominant. Head and back representations were organized topographically across the PPC and M2, and more neurons represented postures that occurred less often. Simultaneous recordings across areas were sufficiently robust to decode ongoing behavior and showed that spiking in the PPC tended to precede that in M2. Both the PPC and M2 strongly represent posture by using a spatially organized, energetically efficient population code.

More than a century of clinical observations have implicated the posterior parietal cortex (PPC) and related networks as essential for maintaining awareness of the spatial configuration of the body, or "body schema" (1, 2). Consistent with this notion, neurophysiological investigations in head-fixed subjects have identified key roles for the PPC and frontal motor cortices in controlling the positioning of individual effectors, such as the eye, arm, or hand (3–10). Parallel studies in rodents have demonstrated ostensibly similar functions for the PPC and frontal motor cortex region M2 in spatial orienting (11), movement planning (12–14), and navigation (15–17), but the field still lacks a quantitative understanding of how the cortex represents posture in freely behaving individuals.

We therefore tracked the heads and backs of 11 rats in three dimensions while recording neural ensembles with dual microdrives targeting deep (>500 μm) layers of the PPC and M2, which exhibit thalamic, cortical, and subcortical connections similar to those of the PPC and premotor areas across mammals (16–18). We recorded 729 well-isolated single units in the PPC and 808 units in M2 during 20-min foraging sessions in a 2-m octagonal arena (fig. S1 and movie S1).

By measuring Euler angles (pitch, azimuth, and roll) of the head, pitch and azimuthal flexion of the back, and neck elevation in an egocentric reference frame (Fig. 1A and methods), we found robust tuning curves for all postural features in the PPC and M2, with peak rates often >5 standard deviations (SD) from the shuffled distribution (Fig. 1, B to G). The majority of cells with tuning peaks exceeding the 99th percentile of the shuffled data (fig. S3, A and B) were stable

across recording sessions (mean of 56.4% in the PPC and 57.8% in M2) (Fig. 1, B to G, and table S1). Postural tuning was also stable across light and dark sessions (fig. S4), indicating its independence from allocentric landmarks and visually oriented attention (18).

Cells in the PPC and M2 frequently responded to conjunctive postures involving the head, back, or whole body (Fig. 2, A and C, and movies S2 to S6), prompting us to build a generalized linear model (GLM) (methods) to identify features best explaining neural activity. We utilized a forward-search procedure in which egocentric posture variables and their derivatives, as well as allocentric features including head direction, running direction, and spatial location, were added until the cross-validated model performance no longer improved significantly (19) (methods).

This approach indicated that the largest fractions of cells in the PPC ($n = 237$, 32.5% of 729 cells) and M2 ($n = 316$, 39.1% of 808 cells) were driven by postural features of the head, including interactions (e.g., between pitch and azimuth), conjunctions of head posture and neck height, and movement (Fig. 2, B and D). Substantial fractions of cells were also tuned to back posture or movement ($n = 69$, 9.5% in the PPC; $n = 75$, 9.3% in M2), as well as elevation or movement of the neck ($n = 43$, 5.9% in the PPC; $n = 84$, 10.4% in M2) (Fig. 2, B and D, and table S2). Smaller percentages of cells exhibited whole-body tuning, being driven by combinations of head, neck, and back angles [$n = 29$, 4.0%, $Z = 7.9$, $P < 0.001$ in the PPC (large-sample binomial test with expected null probability P_0 of 0.01); $n = 27$, 3.3%, $Z = 6.5$, $P < 0.001$ in M2].

Running speed ($n = 38$ cells, 5.2% in the PPC; $n = 26$ cells, 3.2% in M2) and self-motion ($n = 15$ cells, 2.1%, $Z = 2.7$, $P < 0.01$ in the PPC; $n = 4$ cells, 0.5%, $Z = -1.3$, $P > 0.95$ in M2) (Fig. 2, B and D; fig. S5; and table S2) accounted for considerably less of the population than posture (fig. S5). Weaker still were allocentric signals, including head and running direction ($Z = -0.67$, $P > 0.85$

in the PPC; $Z = -0.56$, $P > 0.81$ in M2) and spatial location ($Z = -2.16$, $P > 0.99$ in the PPC; $Z = 0.86$, $P > 0.19$ in M2), which did not reach significance in either area (Fig. 2, B and D, and table S2).

The statistical model indicated that the main features driving cells in the PPC and M2 related to posture (46.2% in the PPC; 58.7% in M2) as opposed to movement (5.6% in the PPC; 3.6% in M2). We tested this further by splitting recording sessions on the basis of movement velocity or posture and found that tuning curves for posture remained virtually identical regardless of movement status, whereas tuning to movement varied unreliably when split by posture (fig. S6). Postural tuning was thus expressed independently of movement, but not vice versa.

Previous studies showed anatomical organization for body and facial movement in parietal and motor areas in various mammalian species (20–23), so we assessed whether postural tuning was also topographical. Head representation in M2 was concentrated at anterior [$\chi^2(4) = 57.1$, $P < 0.001$; Yates corrected χ^2 test] (Fig. 3A) and medial [$\chi^2(4) = 110.6$, $P < 0.001$] locations, whereas back posture predominated at the posterior [$\chi^2(4) = 98.1$, $P < 0.001$] and lateral [$\chi^2(4) = 105$, $P < 0.001$] poles (Fig. 3, A and B). In the PPC, anteromedial sites adjacent to M2 showed the strongest back tuning [$\chi^2(3) = 29.9$, $P < 0.001$, anterior-posterior gradient; $\chi^2(4) = 12.5$, $P < 0.05$, medial-lateral], whereas posterior-lateral regions responded primarily to head posture [$\chi^2(4) = 47.5$, $P < 0.001$, anterior-posterior; $\chi^2(4) = 52.4$, $P < 0.001$, medial-lateral], producing a coarse mirroring of head and back representation across the PPC and M2 (Fig. 3A).

Because the PPC and frontal motor cortices form an extended network supporting spatial movement planning and decision-making (24–27), we asked whether structured correlations existed between spikes recorded simultaneously across areas ($n = 5$ rats). We screened for cells with significant interregional signal correlations (methods) and identified 1017 positively and 182 negatively correlated pairs in one recording session ($n = 15$ sessions) and 758 positively and 141 negatively correlated pairs in a second session ($n = 14$ sessions) the same day. The average normalized positive cross correlations indicated a consistent peak, with the PPC preceding M2 by 50 ms across sessions [–72 ms, –32 ms, bootstrapped 99% confidence interval (CI) for session one; –71 ms, –31 ms for session two] and negative correlations peaking at –85 ms [–190 ms, +16 ms] in session one and –25 ms [–140 ms, +82 ms] in session two (Fig. 3, C and D).

To next address whether population activity was sufficient to reconstruct behavior, we reduced the behavioral dataset from six dimensions (three axes for the head, two for the back, and one for neck elevation) to two by using Isomap (28). This rendered posture for the head, back, and neck on a two-dimensional (2D) surface, or "posture map," with each pixel corresponding to a particular bodily configuration (fig. S7). We chose a session with 37 PPC and 22 M2 neurons recorded simultaneously to train a uniform prior decoder to

Kavli Institute for Systems Neuroscience, Norwegian University of Science and Technology, NO-7489 Trondheim, Norway.
*These authors contributed equally to this work.
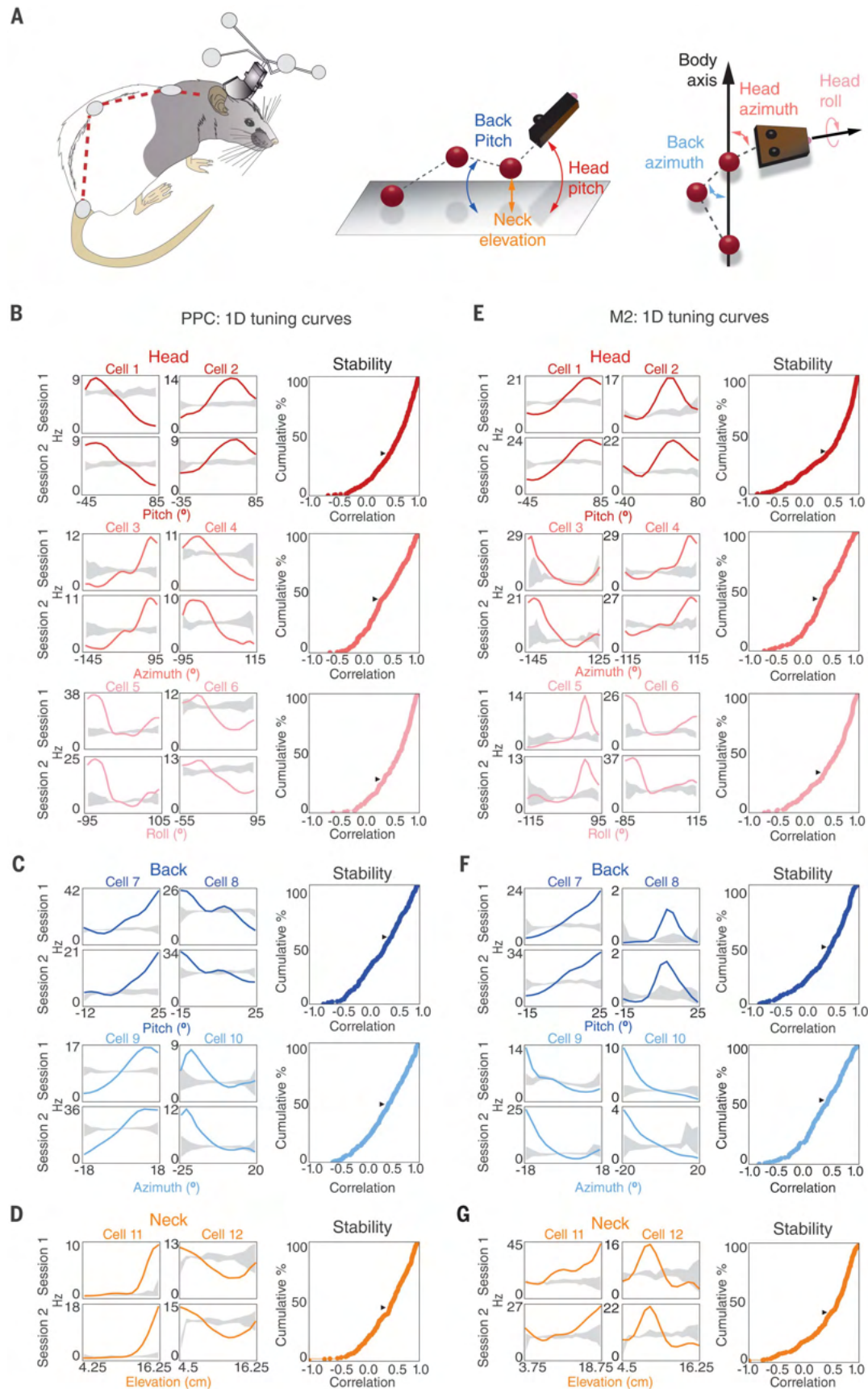†Corresponding author. Email: bartul.mimica@ntnu.no (B.M.); whitlock@ntnu.no (J.R.W.)

Fig. 1. The PPC and M2 show stable 1D tuning curves for postural features of the head, back, and neck. (**A**) (Left) Schematic for the head and three markers along the back (methods and fig. S1). (Middle) Back pitch (blue arrow), neck elevation (orange arrow), and head pitch (red arrow) were calculated relative to the arena floor. Red spheres represent the markers along the back. (Right) Azimuths of the head (dark pink arrow) and back (blue arrow) were measured relative to the body axis vector, from the tail to the base of the neck. Head roll (light pink arrow) was calculated relative to the arena floor. (**B**) (Left) 1D tuning curves for PPC cells for head posture, measured in two open-field sessions, with the 95% CI for shuffled data shown in gray. (Right) Cumulative frequency curves for tuning stability for each feature (arrowheads mark the 95th percentile of the null distribution; detailed results are in table S1). (**C**) (Left) Tuning curves for back pitch (top) and azimuth (bottom). (Right) Across-session stability. (**D**) Same as (C) but for neck elevation. (**E** to **G**) Same as (B) to (D) but for M2.

predict the animal's dynamic position on the posture map on withheld segments (Fig. 4A and movies S7 and S8). Decoder performance, on average, exceeded the shuffled distribution by >45 SD (Fig. 4B).

Cumulative occupancy on the posture map was dominated by epochs when the animal was on all fours with its head lowered (i.e., foraging) (Fig. 4C, left). We found significantly fewer cells tuned to these high-occupancy, or "default," postures (Fig. 4C, dashed oval), whereas less-visited postures were represented more densely by the ensemble ($t_{10} = 4.82$, $P < 0.01$, Welch's two-sided t test) (Fig. 4D, left). The same pattern was observed across animals ($t_{10} = 7.74$, $P < 0.001$) (Fig. 4D, right, and fig. S8), suggesting that receptive fields were distributed on the basis of occupancy. Despite this anisotropy in representation, decoder performance was significantly better than chance for all postures, with smaller error for high- than for low-occupancy postures ($t_{74} = 6.21$, $P < 0.001$) (Fig. 4E).

The finding that cell populations in parietal and frontal motor cortices represent 3D posture

Fig. 2. The PPC and M2 are tuned to combinations of head, back, and neck positions.
(**A**) Example PPC cells tuned to combinations of head, back, and neck positions. Conjunctive representations produce single-firing fields in the 2D rate maps; maximal firing rates (in hertz) are indicated above each map (top). 3D animal models (bottom) depict postures to which cells were tuned. Cell 1 preferred whole-body flexion and head roll to the right; cell 2 fired during rearing, with firing driven by the interaction of head pitch with neck elevation. (**B**) Distribution of behavioral tuning in the PPC as determined by the GLM (see the color-coded legend and table S2 for detailed results). (**C**) Examples of postural tuning in M2 cells. Cell 3 (top right) fired when the head, back, and neck were raised vertically; cell 4 was tuned to leftward head roll and back flexion during sharp turns. (**D**) Distribution of coding properties for 808 M2 cells.
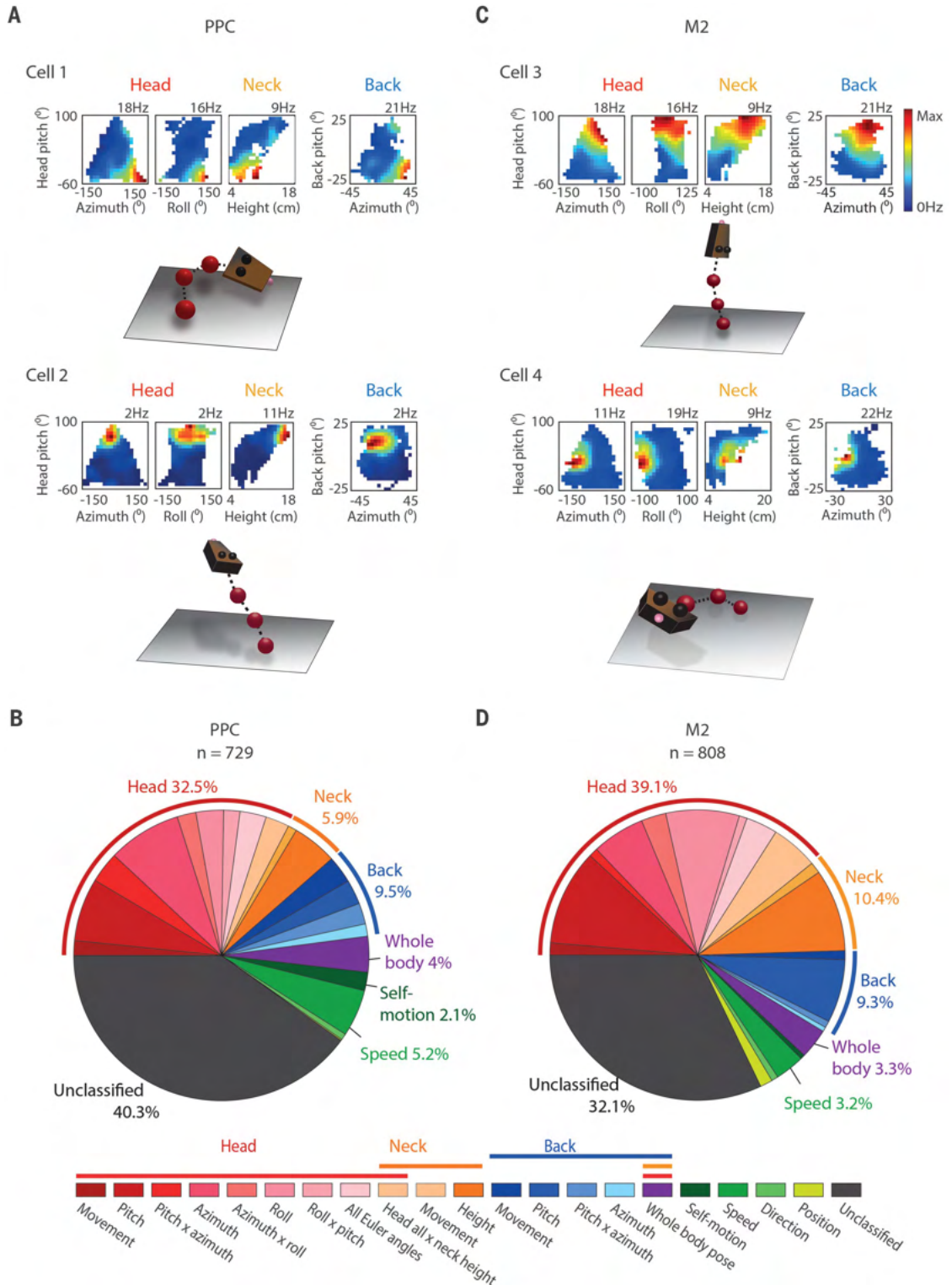
robustly and in larger proportions than other behavioral features complements and extends decades of study on the positional coding of single effectors in stationary animals [e.g., (5, 29–31)]. The predominance of postural tuning in our data

may reflect the myriad kinematic computations that must be solved to coordinate whole-body movement during free behavior. It is also consistent with a functional division of labor in which higher cortical areas specify body position

and goals (32–34) whereas descending motor pathways and subcortical nuclei control movement dynamics more directly (35–39).

The topographical distribution of postural tuning for the head and back appeared to follow
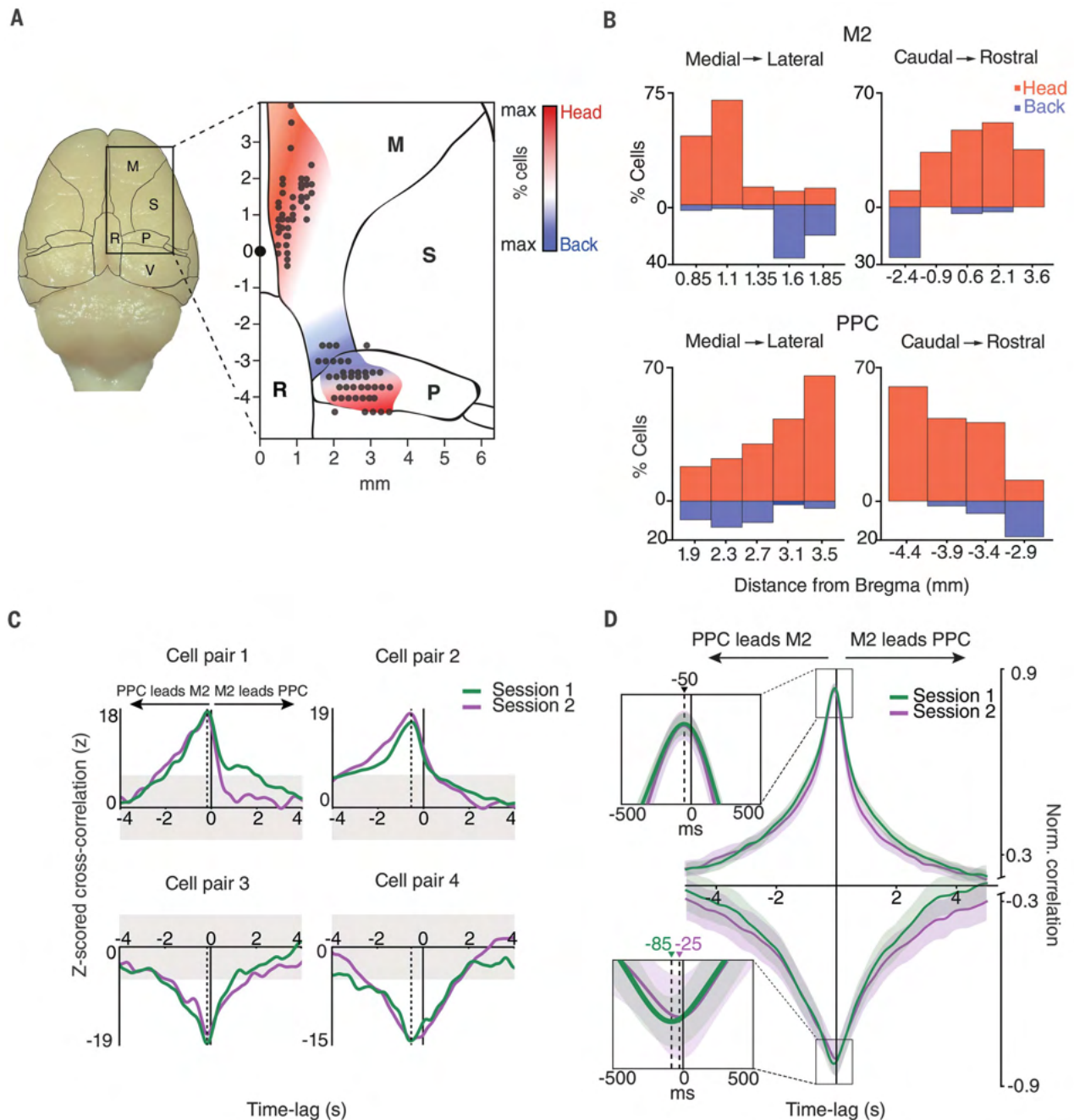
Fig. 3. Head and back posture were organized topographically across the PPC and M2, and the PPC led cross correlations between areas. (A) Dorsal view of the cortex with boundaries delineating primary and secondary motor cortices (M) and somatosensory (S), retrosplenial (R), posterior parietal (P), and visual (V) cortices. The magnified view (right) shows recording locations (gray dots; 41 sites in M2, 40 sites in the PPC), and shading indicates tuning for the head (red) and back (blue). The black dot represents the bregma, with distance marked in millimeters. (B) Percentages of cells in M2 (top) and the PPC (bottom)

driven by head and back positions. For all comparisons, the actual distribution of tuning differed significantly from theoretical distributions that assumed a constant proportion of tuned cells across bins. (C) Four cell pairs in the PPC and M2 showing stable z-scored cross correlations, with the PPC preceding M2. Dashed and solid lines represent the temporal offset of the cross-correlation peaks and time zero, respectively. Gray-shaded areas indicate ±6 SD of the shuffled data. (D) The normalized cross correlation for all cell pairs shows a negative peak for the PPC relative to M2 for positive and negative correlations. Shading indicates the 99% CI.
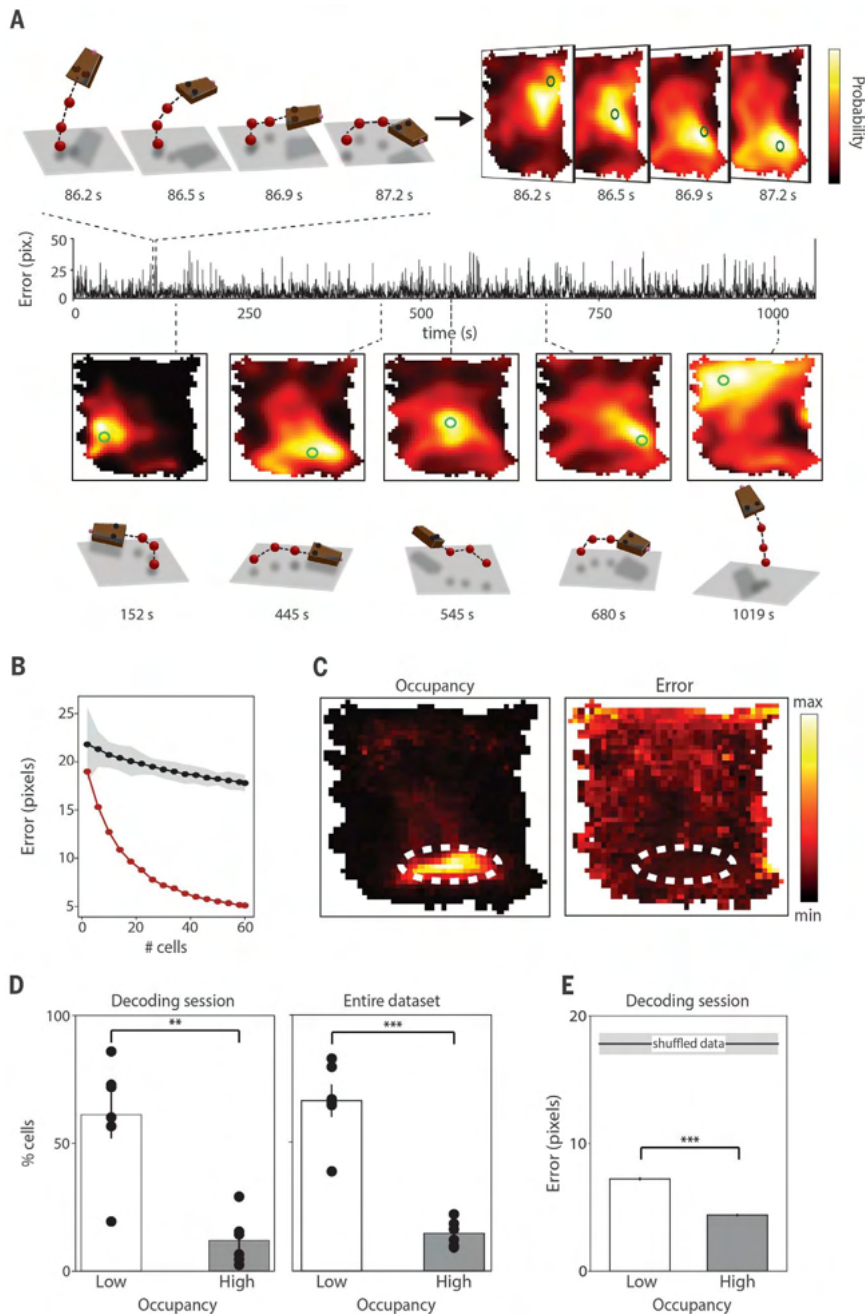
Fig. 4. Ensemble decoding of posture in the PPC and M2 reveals a nonuniform distribution of tuning. (**A**) (Top left) Four snapshots taken within 1 s as the animal came down from rearing and bent rightward. (Top right) Corresponding posture maps illustrate the log posterior distribution of the animal's posture estimated by using PPC and M2 cell ensembles. Actual posture is marked with a green "O," and the maximum likelihood is color coded from yellow to black. (Middle) Timeline indicating error, in Isomap pixels (pix.), over a 20-min recording. (Bottom) Five examples of distinct poses (time points are listed below) and attendant Isomaps illustrating real and decoded postures. (**B**) Decoder accuracy as a function of cell sample size (red dots), with the null distribution above (black dots). The shaded area indicates ±3 SD. (**C**) (Left) Cumulative occupancy on the Isomap showed that the longest dwell times were in the low center of the map, corresponding to foraging. The dashed oval delineates the high-occupancy area where the animal spent >50% of the session. (Right) The average decoding error on the Isomap was smaller in the low center of the map than elsewhere. The dashed oval is the same as in the left panel. (**D**) (Left) The percentage of cells representing the six postural features (black dots) was significantly higher for low- versus high-occupancy bins in the decoding session. (Right) The same analysis for all animals in the study. (**E**) Decoder error was below chance for low- and high-occupancy regions of the posture map and was significantly smaller for the high- than for the low-occupancy area. The line near the top of the graph indicates the mean ± 3 SD for shuffled data. Bar graphs in (D) and (E) indicate mean ± SEM. **$P < 0.01$; ***$P < 0.001$.

a functional organization identified in earlier microstimulation studies in anaesthetized animals (22, 23). We found mainly head and back representation in the PPC and M2, but it is possible that posture for the entire body overlays the cortical surface, including primary somatosensory and motor cortices. More broadly, it remains to be established whether postural signals are generated in the cortex specifically or whether they are inherited from other regions. Our cross-correlation analyses also suggest that a temporal structure exists for postural representations across areas, with the PPC operating upstream from M2, though such an ordering could shift in the context of different tasks (26).

Our use of 3D tracking additionally revealed that speed and self-motion tuning in the PPC (13, 14, 40) were likely overestimated in previous studies using 2D tracking of rodents, owing to insufficient resolution to disambiguate posture from movement. Tracking the back allowed us to detect neural tuning to flexion of the trunk, indicating that vestibular signaling (41) alone could not explain the postural coding in our recordings. For both the back and the head, the arrangement of postural tuning peaks was notably nonuniform and appeared to be optimized for the duration for which postures were occupied (Fig. 4D and figs. S3, A and B, and S8). Previous theoretical works considering optimal coding strategies in sensory systems (42, 43) suggested that the range of the stimulus spectrum visited most should be encoded by more cells with narrower tuning widths, but this was not the case in our data. Rather, we found that proportionately less of the network was dedicated to default states in which the animals spent more time. This arrangement allowed high-fidelity decoding of the entire range of postures while minimizing metabolic demand on the cells, making it both precise and efficient. Together, our results strongly support the notion that the PPC-M2 network plays a key role in representing the dynamic organization of the body in space, or body schema, postulated more than 100 years ago (1, 2).

REFERENCES AND NOTES

1. H. Head, G. Holmes, *Brain* **34**, 102–254 (1911).
2. M. Critchley, *The Parietal Lobes* (Williams and Wilkins, 1953).
3. V. B. Mountcastle, J. C. Lynch, A. Georgopoulos, H. Sakata, C. Acuna, *J. Neurophysiol.* **38**, 871–908 (1975).
4. J. Tanji, E. V. Evarts, *J. Neurophysiol.* **39**, 1062–1068 (1976).
5. R. A. Andersen, V. B. Mountcastle, *J. Neurosci.* **3**, 532–548 (1983).
6. A. P. Georgopoulos, R. E. Kettner, A. B. Schwartz, *J. Neurosci.* **8**, 2928–2937 (1988).
7. J. Wessberg *et al.*, *Nature* **408**, 361–365 (2000).
8. R. A. Andersen, C. A. Buneo, *Annu. Rev. Neurosci.* **25**, 189–220 (2002).
9. M. D. Serruya, N. G. Hatsopoulos, L. Paninski, M. R. Fellows, J. P. Donoghue, *Nature* **416**, 141–142 (2002).
10. M. Hauschild, G. H. Mulliken, I. Fineman, G. E. Loeb, R. A. Andersen, *Proc. Natl. Acad. Sci. U.S.A.* **109**, 17075–17080 (2012).
11. B. Kolb, R. J. Sutherland, I. Q. Whishaw, *Behav. Neurosci.* **97**, 13–27 (1983).
12. J. C. Erlich, M. Bialek, C. D. Brody, *Neuron* **72**, 330–343 (2011).
13. B. L. McNaughton *et al.*, *Cereb. Cortex* **4**, 27–39 (1994).
14. J. R. Whitlock, G. Pfuhl, N. Dagslott, M. B. Moser, E. I. Moser, *Neuron* **73**, 789–802 (2012).
15. D. A. Nitz, *Neuron* **49**, 747–756 (2006).

16. C. D. Harvey, P. Coen, D. W. Tank, *Nature* **484**, 62–68 (2012).
17. A. A. Wilber, B. J. Clark, T. C. Forster, M. Tatsuno, B. L. McNaughton, *J. Neurosci.* **34**, 5431–5446 (2014).
18. E. B. Cutrell, R. T. Marrocco, *Exp. Brain Res.* **144**, 103–113 (2002).
19. K. Hardcastle, N. Maheswaranathan, S. Ganguli, L. M. Giocomo, *Neuron* **94**, 375–387.e7 (2017).
20. J. Hyvärinen, *Brain Res.* **206**, 287–303 (1981).
21. I. Stepniewska, P. C. Fang, J. H. Kaas, *Proc. Natl. Acad. Sci. U.S.A.* **102**, 4878–4883 (2005).
22. R. D. Hall, E. P. Lindholm, *Brain Res.* **66**, 23–38 (1974).
23. M. Brecht *et al.*, *J. Comp. Neurol.* **479**, 360–373 (2004).
24. S. P. Wise, D. Boussaoud, P. B. Johnson, R. Caminiti, *Annu. Rev. Neurosci.* **20**, 25–42 (1997).
25. G. Rizzolatti, L. Fogassi, V. Gallese, *Curr. Opin. Neurobiol.* **7**, 562–567 (1997).
26. B. Pesaran, M. J. Nelson, R. A. Andersen, *Nature* **453**, 406–409 (2008).
27. T. D. Hanks *et al.*, *Nature* **520**, 220–223 (2015).
28. J. B. Tenenbaum, V. de Silva, J. C. Langford, *Science* **290**, 2319–2323 (2000).
29. P. R. Brotchie, R. A. Andersen, L. H. Snyder, S. J. Goodman, *Nature* **375**, 232–235 (1995).
30. A. P. Batista, C. A. Buneo, L. H. Snyder, R. A. Andersen, *Science* **285**, 257–260 (1999).
31. E. Salinas, P. Thier, *Neuron* **27**, 15–21 (2000).
32. G. H. Mulliken, S. Musallam, R. A. Andersen, *J. Neurosci.* **28**, 12913–12926 (2008).
33. L. Fogassi *et al.*, *J. Neurophysiol.* **76**, 141–157 (1996).
34. T. M. Pearce, D. W. Moran, *Science* **337**, 984–988 (2012).
35. G. M. Shepherd, *Nat. Rev. Neurosci.* **14**, 278–291 (2013).
36. G. Cui *et al.*, *Nature* **494**, 238–242 (2013).
37. J. J. Wilson, N. Alexandre, C. Trentin, M. Tripodi, *Curr. Biol.* **28**, 1744–1755.e12 (2018).
38. M. S. Esposito, P. Capelli, S. Arber, *Nature* **508**, 351–356 (2014).
39. J. E. Markowitz *et al.*, *Cell* **174**, 44–58.e17 (2018).
40. X. Chen, G. C. Deangelis, D. E. Angelaki, *Neuron* **80**, 1310–1321 (2013).
41. F. Klam, W. Graf, *Eur. J. Neurosci.* **18**, 995–1010 (2003).
42. N. S. Harper, D. McAlpine, *Nature* **430**, 682–686 (2004).
43. D. Ganguli, E. P. Simoncelli, *Neural Comput.* **26**, 2103–2134 (2014).
44. B. Mimica, Efficient cortical coding of 3D posture in freely behaving rats – data and GUI, Norstore (2018); https://doi.org/10.11582/2018.00028.

ACKNOWLEDGMENTS

SUPPLEMENTARY MATERIALS

Science

Efficient cortical coding of 3D posture in freely behaving rats

Bartul Mimica, Benjamin A. Dunn, Tuce Tombaz, V. P. T. N. C. Srikanth Bojja and Jonathan R. Whitlock

Posture in the brain

Our understanding of the neural basis of motor control originates in studies of eye, hand, and arm movements in primates. Mimica *et al.* investigated neuronal representations of body postures in the posterior parietal and frontal motor cortices with three-dimensional tracking of freely moving rodents (see the Perspective by Chen). Both brain regions represented posture rather than movements and self-motion. Decoding the activity of neurons in the two regions accurately predicted an animal's posture.
Science, this issue p. 584; see also p. 520

ARTICLE TOOLS	http://science.sciencemag.org/content/362/6414/584
SUPPLEMENTARY MATERIALS	http://science.sciencemag.org/content/suppl/2018/10/31/362.6414.584.DC1
RELATED CONTENT	http://science.sciencemag.org/content/sci/362/6414/520.full
REFERENCES	This article cites 48 articles, 11 of which you can access for free http://science.sciencemag.org/content/362/6414/584#BIBL
PERMISSIONS	http://www.sciencemag.org/help/reprints-and-permissions

Use of this article is subject to the Terms of Service

Supplementary Materials for

Efficient cortical coding of 3D posture in freely behaving rats

Bartul Mimica*†, Benjamin A. Dunn*, Tuce Tombaz, V. P. T. N. C. Srikanth Bojja,
Jonathan R. Whitlock†

*These authors contributed equally to this work.
†Corresponding author. Email: bartul.mimica@ntnu.no (B.M.); whitlock@ntnu.no (J.R.W.)

This PDF file includes:

Other Supplementary Material for this manuscript includes the following:
(available at www.sciencemag.org/content/362/6414/584/suppl/DC1)

27 **Materials and Methods**

28 <u>Subjects and electrode implantation.</u>

29 Experiments were performed in accordance with the Norwegian Animal Welfare Act and the

30 European Convention for the Protection of Vertebrate Animals used for Experimental and

31 Other Scientific Purposes. The study contained no randomization to experimental

32 treatments and no blinding. Sample size (number of animals) was set a priori to two or

33 more, considered as the minimum required to obtain the number of cells needed for

34 statistical analysis of the present type of data. No statistical method was used to

35 predetermine sample size. Neuronal activity was recorded from nine male and two female

36 Long-Evans rats (3–5 months old, 400–600 g) with chronically implanted dual microdrives. A

37 silicon probe (NeuroNexus Inc., MI, USA; custom design based on A8x1-tet-2mm-200-121)

38 was mounted on each microdrive. One probe targeted PPC (-3.8 to -4.25mm AP, center shank

39 2.7mm ML) and one targeted M2 (center shank +0.5mm AP, 0.7mm ML). Each probe had eight

40 55μm wide, 15μm thick, 2mm long shanks, with four $160μm^2$ iridium recording sites

41 configured as a tetrode at each tip; inter-shank spacing was 200μm. At surgery, animals were

42 anesthetized in a ventilated Plexiglas box with 5% isoflurane vapor, and maintained on 1.0-

43 2.5% isofluorane for the duration of surgery. Body temperature was maintained at 37°C with

44 a heating pad. Once unconscious, animals received s.c. injections of analgesic (Metacam

45 2.5mg/kg weight, Temgesic (buprenorphine) 0.05mg/kg). Local anesthetic (Marcain 0.5%)

46 was injected under the scalp before making the incision. The skull was then exposed, rinsed

47 and sterilized using 0.9% saline and 3% hydrogen peroxide. A high-speed dental drill with

48 0.8mm burr was used to drill holes for skull screws and craniotomies over PPC and M2. Bone-

49 tapping stainless steel screws were inserted securely into the skull, with a single screw serving

50 as the ground wire and reference for both drives. The microdrives were housed in a single 3D

51   printed unit that was lowered with probes targeting the right hemisphere. The drive unit was

52   cemented to the skull, and probes were lowered into the brain, and craniotomies were filled

53   with a 70-30% mixture of mineral oil and low-melt bone wax (Sigma-Aldrich Norway AS, Oslo,

54   Norway). After surgery rats awoke in a 32°C heated chamber, were returned to their home

55   cage, and later administered post-operative analgesics. Rats were housed individually in

56   Plexiglas cages (45 x 44 x 30 cm) in a humidity and temperature-controlled environment, and

57   kept on a 12 hr light/12 hr dark schedule. All training and testing occurred in the dark phase.

58

59   In vivo electrophysiology and behavior.

60   Single units, LFP or raw signal from PPC and M2 were sampled with a Digital Lynx 4SX

61   recording station (Neuralynx Inc. Montana, USA). Rats were connected via AC-coupled unity-

62   gain operational amplifiers above the head (via H32-to-HS36 custom head stages, Neuralynx

63   Inc.), which connected to a motorized commutator above the arena. Elastic string was used

64   to counterbalance weight and excess cable length, allowing animals to move freely in the

65   recording arena.

66   Silicon probes were lowered in 50μm steps while the rat rested on a towel in a flower

67   pot on a pedestal. Turning stopped when well-separated units appeared, typically between

68   500 and 1800μm. Data collection started when signal amplitudes exceeded ~4 times the noise

69   level (r.m.s. 20-30μV) and units were stable for > 3hr. After recording at a given depth, PPC

70   and M2 probes were lowered to obtain new cells; probe depths typically differed by 100μm

71   or more between recording days.

72   Behavioral recordings were performed as rats foraged for crumbs of chocolate, cereal

73   or vanilla cookies thrown randomly into an octagonal, black open-field arena (2 × 2 × 0.8 m),

74   with the animals oriented by extra-arena room cues. Recordings began once the animals

75   achieved routine, complete coverage of the arena. Recording sessions typically lasted just

76   over 20 minutes (average length 1335s, total range of 610-2467s). Rats rested a minimum of

77   1 hour in their home cage between runs.

78   Two animals (#23938 and #23939) were expressing rAAV8/CamKII-Jaws-KGC-GFP-ER2

79   after bilateral injections to M2, but no light was activated during the reported recording

80   sessions.

81

82   <u>Spike sorting and analysis of firing rates during behavior.</u>

83   For the first six rats, spike data were clustered automatically with KlustaKwik (K. Harris,

84   http://klustakwik.sourceforge.net/) then sorted manually using graphical cluster-cutting

85   software *(45)*. For the remaining five animals, raw signal Neuralynx files collected on the same

86   recording day were converted to binary format and concatenated, such that the identity of

87   isolated units could be preserved across sessions. Spike sorting was performed offline with

88   Kilosort   (*46*),   followed   by   manual   curation   in   Phy   (C.   Rossant,

89   https://github.com/kwikteam/phy). Clusters were merged or separated based on waveform

90   similarity, spike rate auto- and cross-correlation and masked cluster quality measures.

91   Clusters with ≥ 2% violation of a 2ms inter-spike interval were discarded. After spikes were

92   split into individual sessions for each cluster, only cells with >100 spikes per session were kept

93   for further analyses.

94

95

96

97   3D tracking and model assignment.

98   For tracking the head, four 9mm retroreflective markers (ca. 6cm apart) were affixed to a rigid

99   body clamped above the recording drives. For the back, three 9mm circular cut outs of

100   retroreflective tape (3M) were each affixed to shaved locations at the shoulder blades, the

101   hunch of the back, and above the root of the tail. Position data were recorded at 120 fps using

102   a 6-camera infrared recording system (OptiTrack, Oregon, USA), and registered using optical

103   motion capture software (Motive, version 1.8, 1.9 or 1.10.2; OptiTrack).

104   For seven of 11 animals (tracked with Motive versions 1.9 or 1.10.2), labeling of

105   individual markers was performed with the in-built labelling functions in Motive on raw .tak

106   files. Specifically, the 3D data was first deleted. Then, a rigid body was constructed from the

107   four head markers (in the same way across animals), and the three body markers were kept

108   in a separate marker set. Both marker assets were then dragged onto the take and the

109   "reconstruct and autolabel" function was applied. Depending on the results, errors in marker

110   assignment were corrected and the unlabeled points were hand labelled. The percentage of

111   the sessions for which individual markers (across animals, across sessions) was tracked were

112   as follows: 98.51% above the base of the tail (total range: 91-99%), 97.66% for the middle of

113   the back (total range: 87-99%), and 96.33% for between the shoulder blades (total range: 83-

114   99%). For each of the head markers, the mean percentages were 99% for head 1 (total range:

115   99-99%), 98.78% for head 2 (total range: 85-99%), 98.61% for head 3 (total range: 88-99%)

116   and 98.89% for head 4 (total range: 95-99%). The head as a whole was captured 98.82% of

117   the time (total range: 85-99%). After each session was labeled, remaining unlabeled markers

118   were deleted and the data were exported as a .csv file, with units in meters and individual

119   markers (not rigid body) as output. A brief, custom-written Python script was used to convert

120   the .csv file into a .pkl file, which was modified for usage in a custom graphical user interface

121   (GUI). In the GUI, the head coordinate system was constructed and the tracking data was

122   merged with spike data for further processing.

123   For the remaining four animals (tracked using Motive version 1.8), raw data was

124   exported as a .csv file, with units in meters and individual markers as output. The .csv file was

125   then loaded into the GUI and each point was hand labelled for > 90% of the time it was tracked

126   each session. The mean number of frames across all open field sessions was 160159.1 (total

127   range: 73231-296021).

128   For all animals, files containing tracked points were loaded into the GUI, where the

129   coordinate system for the rigid body on the head was translated to minimize jitter, which

130   roughly corresponded to placing it at the base of the head. We then rotated the coordinate

131   system such that, on average, the x-direction of the head closely matched the horizontal

132   movement direction.

133

134   <u>Extracting behavioral variables from tracking data.</u>

135   Following the recording, we labelled tracked points within the Motive (OptiTrack) interface,

136   and imported the labelled data into a custom script in Fiji. Using the four tracked points on

137   the animal's head, we estimated the geometry of the rigid body using the average pairwise

138   distances between markers. We then found the time point at which this geometry was closest

139   to the average, and used that time point as a template. We then assigned an XYZ coordinate

140   system to the template with the origin located at the centroid of the four points, and

141   constructed coordinate systems at each time point of the experiment by finding the optimal

142   rigid body transformation (*47*) of the template to the location of the head markers. In order

143   to find the likely axis of rotation for the head (i.e. the base of the head), we found the

144   translation of the coordinate system that minimized the Euclidean distance between the

145   origin at time point t-20 and t+20, where t is measured in frames from the tracking system

146   (120 Hz). Next, the coordinate system was rotated to most closely match the Z-direction with

147   the vertical direction of the room, and X-direction with that of the running direction, which

148   was defined by horizontal movements of the origin from t-50 to t+50. Only time points where

149   speed exceeded 10 cm/s were used to estimate running direction. The two objectives were

150   combined by considering the sum of squared differences of the two sets of angles. This

151   definition of running direction was used only to rotate the head direction, and was not used

152   in subsequent analyses. Hyperparameters were chosen such that head placement using the

153   resulting coordinate system visibly matched experiments.

154   To compute the variables for relating tracking to neural activity, we first denoted body

155   direction as the horizontal component of the vector from the marker on the animal's rear to

156   the neck point. The angles of the head (pitch, azimuth and roll) relative to body direction were

157   then computed assuming the XYZ Euler angle method. The back angles (pitch and azimuth)

158   were determined relative to body direction using standard 2D rotations, which were optimally

159   rotated such that the average peak of the occupancy was close to zero. The point on the neck

160   was then used to determine neck elevation relative to the floor, as well as the horizontal

161   position of the animal in the environment. Movement variables were estimated from the

162   tracked angles using a central difference derivative with a time offset of 10 bins. Running

163   speed was then estimated using a moving window of radius 15 bins. The values for self-motion

164   were computed as the speed of the animal multiplied by the X and Y component of the

165   difference in angles between the body direction at t-15 and t+15. We found this a more

166   reliable representation of self-motion compared to previous mathematical descriptions (*14*).

167   <u>1D tuning curves.</u>

168   Angular behavioral variables were binned in 5°, with exception of back angles, which were

169   lowered to 2.5°. Movement variables were binned in 36 equally-spaced bins, spanning the

170   range of recorded variables such that there was a minimum occupancy of 400 milliseconds in

171   both the first and last bins. Neck elevation bins were 1cm, while position in the environment

172   was estimated using 6.67cm bins. Finally, self-motion used a bin size of 3cm/s. For all rate

173   maps, the average firing rate per bin was calculated as the total number of spikes per bin,

174   divided by total time spent in the bin. All smoothed rate maps were constructed with a

175   Gaussian filter with standard deviations of 1 bin. Only bins with a minimum occupancy of 400

176   milliseconds were used for subsequent analysis. To compare with shuffled distributions, we

177   shifted the neural activity 1000 times on the interval of ±[15,60] seconds.

178

179   <u>Model selection.</u>

180   To determine which of the large number of tracked features best explained the neural activity

181   we considered the neural activity binned to match the resolution of the tracking system (120

182   Hz). We fit the neural data using a Bernoulli generalized linear model (*48*) assuming different

183   versions of the natural parameter for each neurons, where each version contained a feature

184   or sets of features as well as the constant term. We included each of the six postural features,

185   their derivative values, body direction, head direction, speed, position and self-motion each

186   in single variable models. We then maximized the likelihood of the data given each of the

187   models using an L1 regularizer with $\lambda = 10^{-4}$ for each model across 10 folds of the data. We

188   tested all combinations of angles associated with the head, back, and a model with all six

189   behavioral variables.

190   We first compared the single feature models using the average cross-validated log-

191   likelihood ratio, keeping the model, if any, that had the highest positive score and was

192   significantly different from zero *(19)*. Significance was determined using a one-sided Wilcoxon

193   signed rank test with significance of 0.01. Additional features were included if the increase in

194   cross-validated log-likelihood ratio of the more complicated model was significantly more

195   than that of the less-complicated model. Significance was again determined using a one-sided

196   signed rank test with significance value of 0.01.

197

198   Cross-correlations.

199   In sessions with dual simultaneous recordings, firing rates were calculated for each cell in 5ms

200   bins and smoothed with a Gaussian kernel (SD = 100ms). Pairwise cross-correlations

201   (Pearson's *r*) were computed between the activity of any given M2 cell with each of the

202   simultaneously-recorded PPC cells by offsetting the spiking activity of the PPC cell at intervals

203   of 5ms from -5 to 5 seconds. To obtain values for the null-distribution, the first cell pair was

204   cross-correlated 1000 times with a random offset each time, ranging from ±20 to 40 seconds.

205   Pairs were considered to be significant if their peak cross-correlation was greater than 0.1 (in

206   absolute terms) and if they exceeded chance values by six SD for 200ms, centered at the peak.

207   The example pair cross-correlations were z-scored, so session 1 and 2 could be shown on the

208   same scale. Group results were obtained by normalizing all significant cross-correlations

209   series by the absolute value of their peak and then averaging them at every time point. The

210   grey shaded area represents the 99% CI for the resulting mean values. Bootstrapped values

211   for the peaks were generated by resampling with replacement from the cross-correlation sets

212   1000 times with significant positive or negative series. For each of the bootstraps, obtained

213   series were normalized by the absolute value of their peak and then averaged at every time

214   point. For each of the 1000 samples, we established the temporal offset of the peak/trough

215   in the curve. We calculated the SD of the distribution of the peak/trough offsets and

216   considered that the standard error of the population mean and obtained confidence intervals

217   around bootstrapped means, which corresponded to the observed peaks to the third decimal.

218

219   Decoding.

220   In order to visualize and decode in the space of the six posture variables we used a common

221   dimensionality reduction technique, Isomap (*28*), to reduce the space to two dimensions. We

222   did this by first normalizing each of the features, dividing the values for each by the maximum

223   of the absolute value of the feature. This bounded the angular values to [-1,1] and the neck

224   elevation to [0,1]. We then applied Isomap from the python library Scikit-learn (*49*) with an

225   assumed number of neighbors equal to 100, which resulted in an estimated reconstruction

226   error of 0.03.

227   In order to decode on this space, we again assumed the neural data were distributed

228   according to a Bernoulli distribution and fit it with a GLM. In this case, however, we used a

229   square grid, 22 X 22, of Gaussian functions with width of 0.25 units to serve as a basis set (*50*)

230   for the Isomap surface, spanning the total space of 2.99 X 2.53 units. We used a small L1

231   regularizer with $\lambda = 10^{-7}$ and a 10 fold cross-validation scheme. The number and width of the

232   basis functions as well as the value for the regularizer were determined by optimizing the

233   average log-likelihood of the test sets. After fitting the model to the data, we computed the

234   log-likelihood at each time point of the test data and for each bin of the binned posture map

235   (50 X 50). To then visualize this as a dynamic map, $Q(t,x,y)$, of the animal's likely position (x,y)

236   in this posture space at time t, we let $Q(t,x,y)=\exp(L_{ave}(t,x,y))$, where $L_{ave}(t,x,y)$ was determined

237 from a moving 150ms Gaussian average of the log-likelihood of the test data for each posture

238 bin (x,y). The maps of Q(t,x,y) can be visualized in both Supplementary Videos 7-8 as well as

239 in Figure 4a. Only bins occupied >150ms are displayed in the figures. The most likely position

240 at a given time bin t was then determined by finding the x,y position corresponding to the

241 peak value of Q(t,x,y). The error between the values for x and y and the true position were

242 then computed using the Euclidean distance. This was done for the entire recording of 59

243 neurons as well as with subsets of neurons. To estimate performance with fewer neurons, we

244 built the decoder using random subsets of 2, 6, 10, … 54 and 58 neurons. Decoding was

245 repeated 100 times for each population size to compute a mean decoding accuracy. For each

246 population size, chance values were computed by shuffling the spikes of each neuron

247 independently by a number of ±[10,120] seconds. This procedure was repeated 100 times for

248 each population size. To estimate the likely number of neurons required for perfect decoding

249 of the posture space, we extrapolated a linear fit to the reconstruction error as a function of

250 the log of the number of neurons. Finally, decoder error as a function of bins in the posture

251 map was estimated by taking the average error of the moments the animal was located in a

252 given posture bin.

253

254 Histology.

255 Silicon shanks were left in place after the final recording session. The rats received an

256 overdose of Isofluorane and were perfused intracardially with saline and 10 % formalin or 4%

257 paraformaldehyde. Electrodes were removed 60-120 min after perfusion, and brains were

258 extracted and stored in DMSO. Frozen sagittal sections (30 μm) were cut in a cryostat, all

259 sections were mounted on glass slides and stained with cresyl violet. Using a digital scanner

260 and scanning software (Carl Zeiss AS, Oslo, Norway), electrode locations in PPC and M2 were

261 registered with respect to local anatomical landmarks. Recoding sites were located on

262 photomicrographs obtained using ZEN (blue edition) and imported to Adobe Illustrator. The

263 position of the electrodes during recording was extrapolated using the read-out of the tetrode

264 turning protocol and taking shrinkage (~20%) from histological procedures into account.

265 Recording depths in PPC ranged from 500-1800μm, and in M2 ranged from 500-1800μm.

266

267

A

infrared cameras

2.5m

2m

B

M2-targeting drive

PPC-targeting drive

rostral

lateral

C

B

1mm

- Rat 21082
- Rat 22986
- Rat 22413
- Rat 22412
- Rat 22985
- Rat 22006
- Rat 22100
- Rat 22007
- Rat 22984
- Rat 23939
- Rat 23938

D

Frontal cortex

M2 M1 S1

CG

1mm
+0.5 AP

Posterior parietal cortex

RSA mPPC lPPC

S1

1mm
-3.5 AP
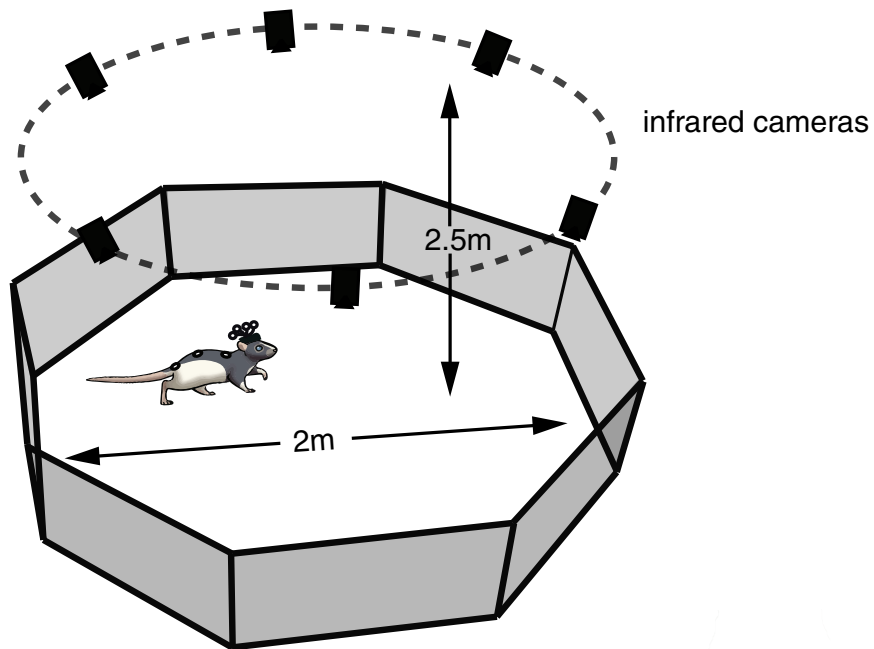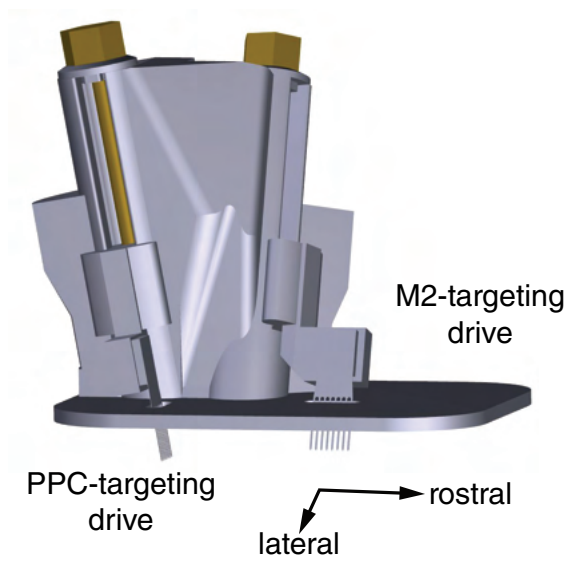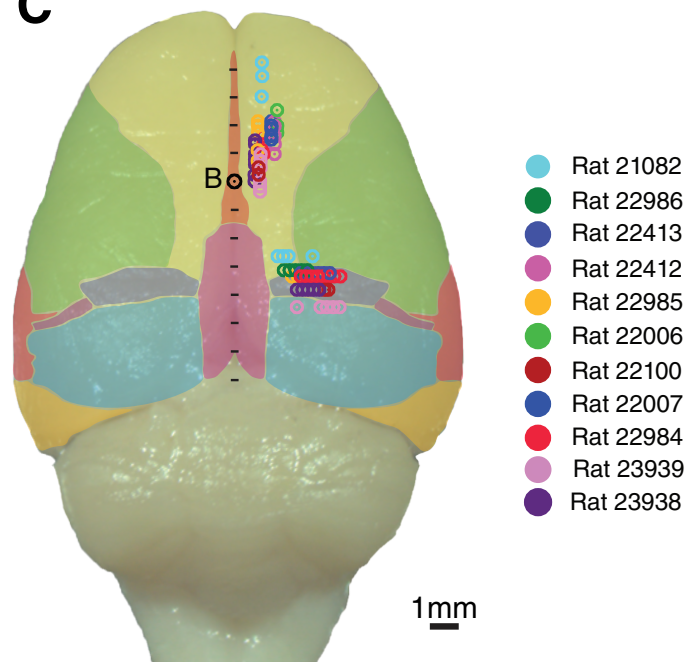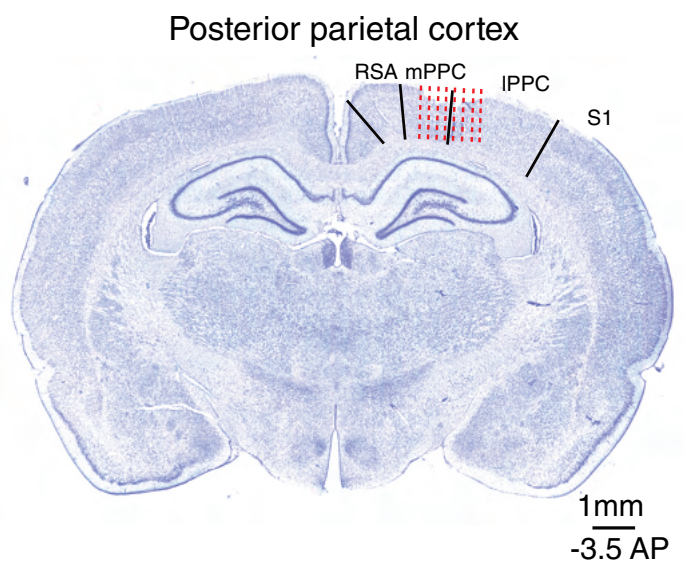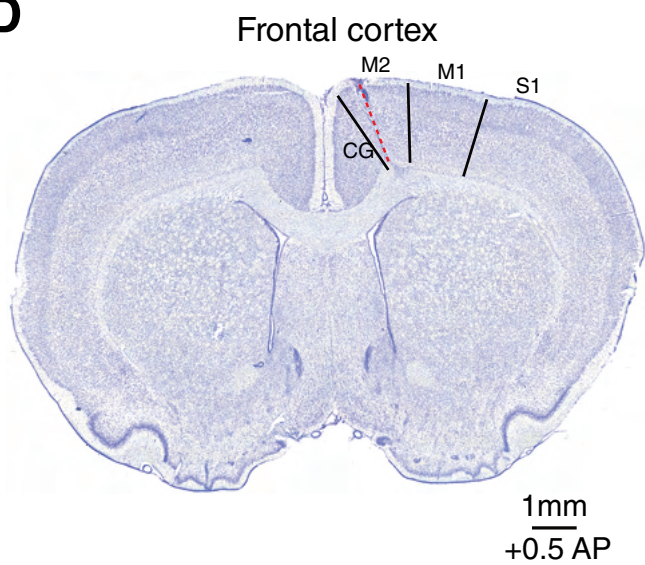
268   **Fig. S1. Experimental methods for 3D tracking and neural recordings.**

269   **(A)** Rats with retroreflective markers on the head and back ran in a 2m open octagonal arena

270   with 6 high-speed (120fps) infrared cameras arranged above in a circle. **(B)** Custom dual

271   microdrives were used to target 8-shank silicon probes to PPC and M2. The M2 drive was

272   designed to target the cortical surface at 0.7 to 0.75mm lateral of midline, and was tilted 20°

273   laterally to maximize travel in M2. The PPC drive was positioned 4mm behind the caudal-most

274   shank on the M2 drive, and was centered 2.7mm lateral of midline. The PPC drive was tilted

275   10° so that shanks advanced rostrally with turning. **(C)** Aerial view of cortical penetrations

276   yielding single units in 11 rats, with brema labeled "B", and tick marks indicating mm.

277   Recording sites for frontal drives ranged from -0.48 to +4.2mm AP, and from ~0.6 to 2.0mm

278   ML. Shanks targeting PPC spanned 1.7 to 3.7mm ML, and -3.0 to -4.5 AP. In two animals the

279   posterior drive penetrated into caudal M2 (see Fig. S2). **(D)** Cresyl violet-stained coronal

280   sections (40μm thick) showing recording tracks (red stippled lines) in M2 (left) and PPC (right).

281

282

283

284

285

286

287

288

289

290

291

292

M2 sites

Anterior

+4.20 mm
+3.72 mm
+3.00 mm
+2.52 mm
+2.16 mm
+1.92 mm
+1.80 mm
+1.68 mm
+1.56 mm

Posterior

+1.44 mm
+1.28 mm
+1.08 mm
+0.96 mm
+0.84 mm
+0.72 mm
+0.60 mm
+0.48 mm
+0.24 mm
0.00 mm
-0.24 mm
-0.48 mm

Anterior

Posterior

PPC sites

-2.64 mm
-3.12 mm
-3.24 mm
-3.36 mm
-3.96 mm
-4.44 mm

Anterior

Posterior
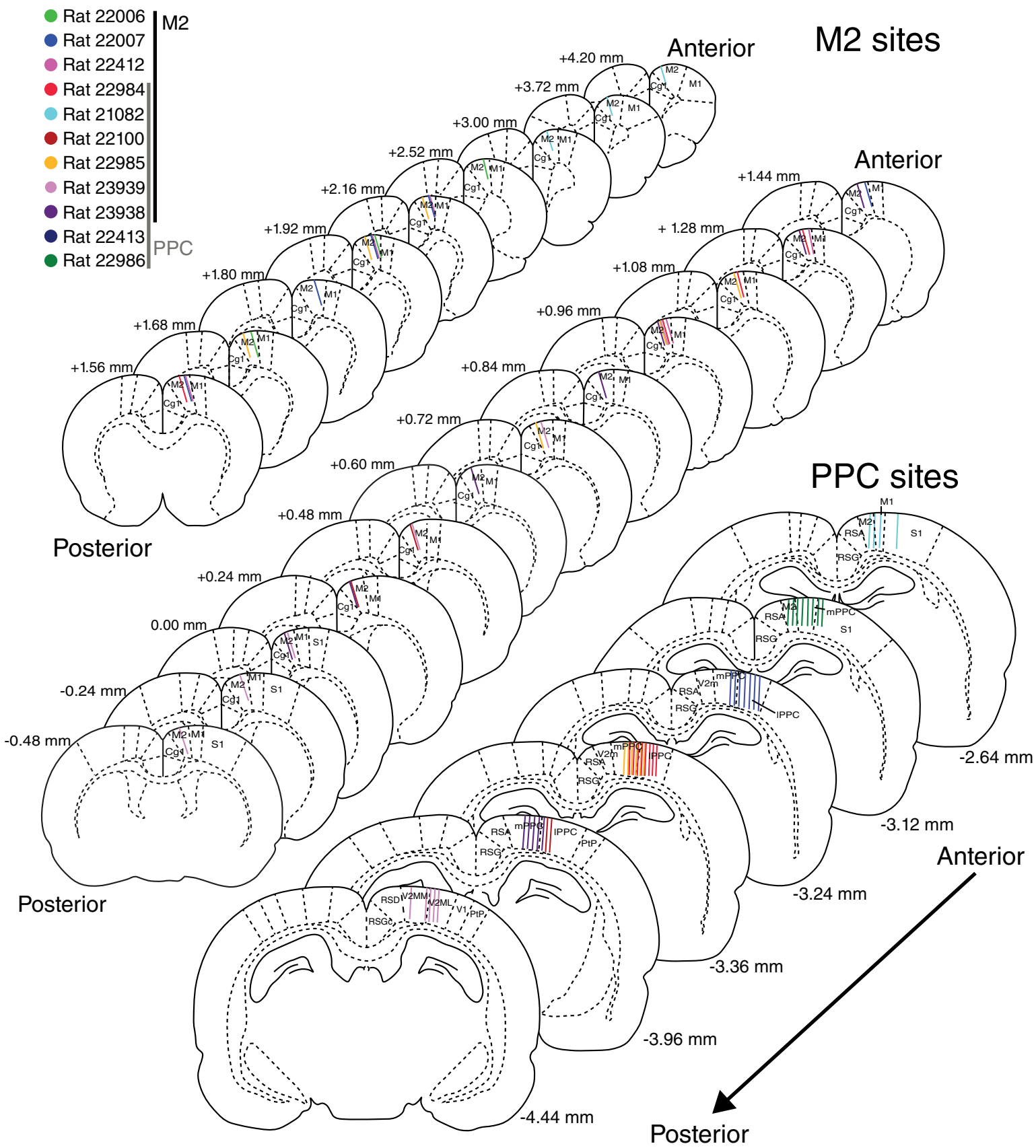
293 **Fig. S2. Recording locations of each shank that produced single units.**

294 Top two rows of maps ("M2 sites") show architectonic boundaries at each AP location in nine

295 rats where an M2-targeting drive recorded single units. Recording locations in M2 ranged

296 from +4.20mm to -0.48mm AP; all recording sites were confirmed histologically as inside M2.

297 The bottom row ("PPC sites") shows coronal maps where single units were recorded in PPC

298 and neighboring regions in eight rats. Recordings spanned the rostral-caudal extent of PPC,

299 and in one animal (#23939) included area V2M *(51)*. Probes in two rats (#21082 and #22986)

300 had shanks at sites rostral to PPC, resulting in units recorded in caudal M2. Ten units in rat

301 #21082 were recorded in M1 and analyzed separately.

302
303
304
305
306
307
308
309
310
311
312
313
314
315
316
317

318

A PPC tuning peak distribution
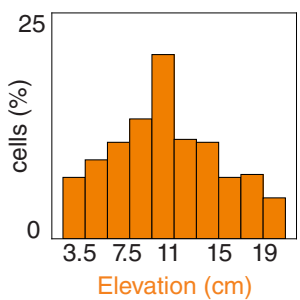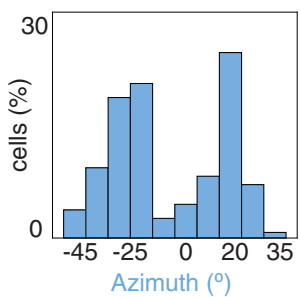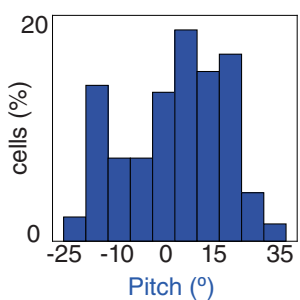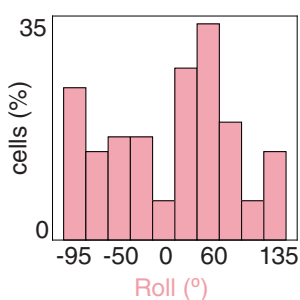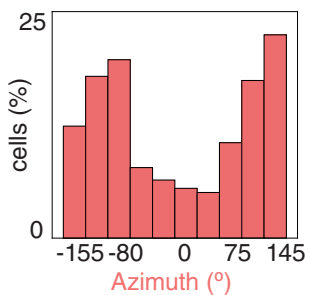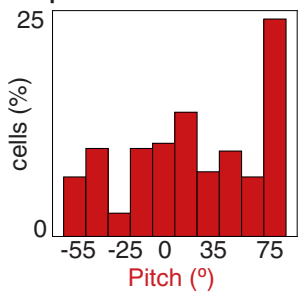
B M2 tuning peak distribution

C Occupancy

Head

Pitch (°)

Azimuth (°)

Roll (°)

Back

Pitch (°)

Azimuth (°)

Neck

Elevation (cm)
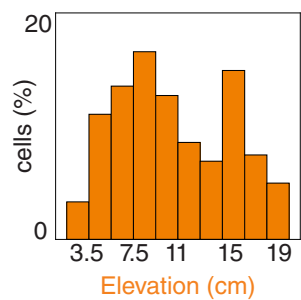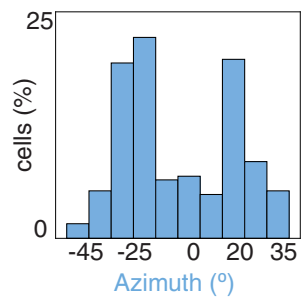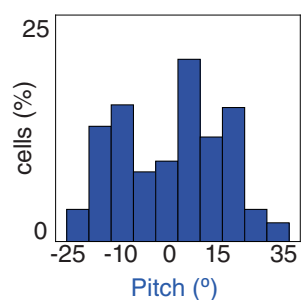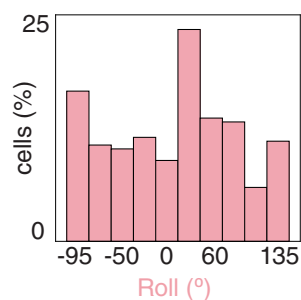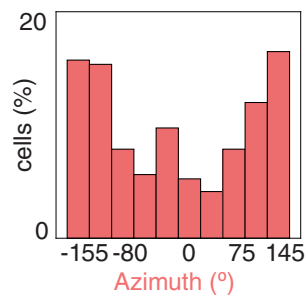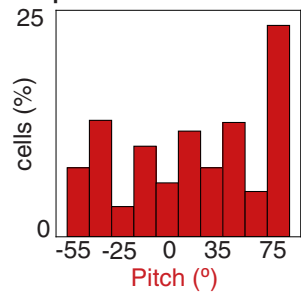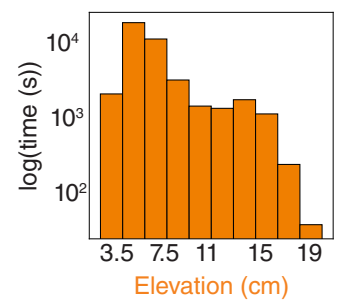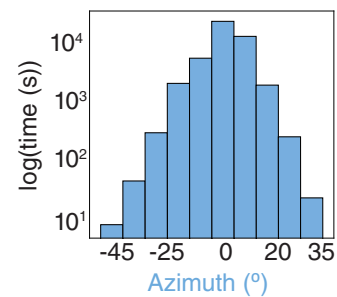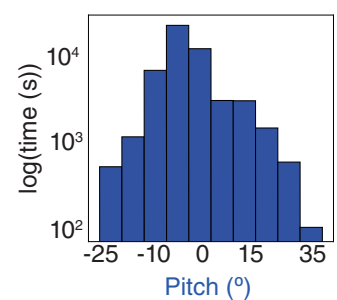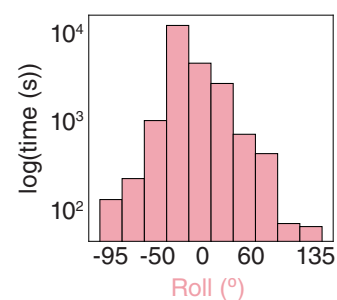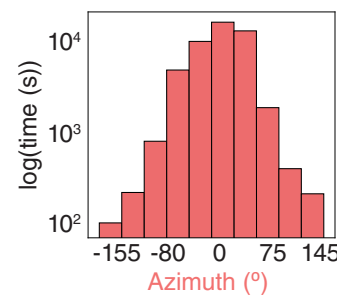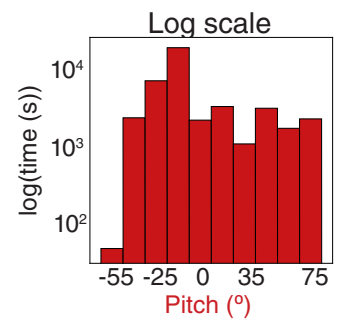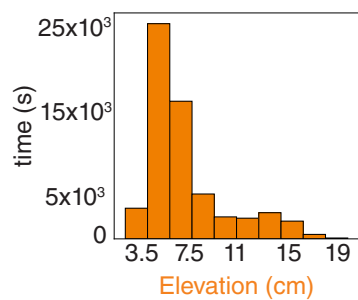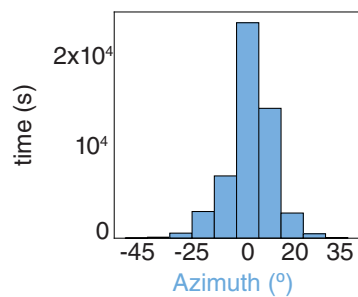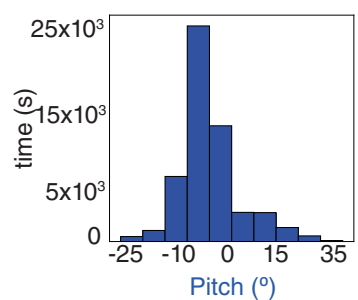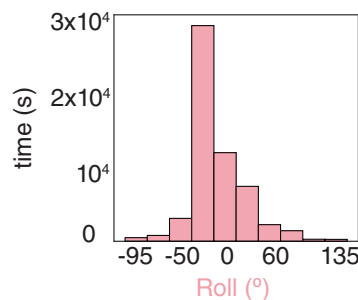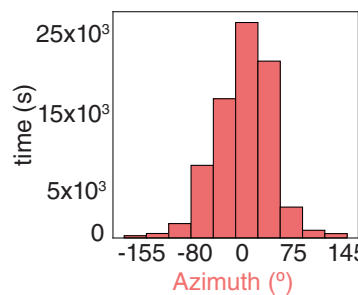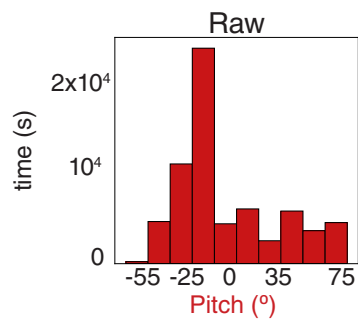
319 **Fig. S3. Tuning peak distributions in PPC and M2, and behavioral coverage.**

320 **(A**) The distribution of tuning peaks for head, back and neck position in PPC. For all features

321 tested, the observed distributions of tuning peaks were significantly non-uniform (top to

322 bottom: head pitch, $\chi^2(9)$ = 104.3, P <0.001; head azimuth, $\chi^2(9)$ = 64.8, P < 0.001; head roll,

323 $\chi^2(9)$ = 50.8, P < 0.001; back pitch, $\chi^2(9)$ = 113.7, P < 0.001; back azimuth, $\chi^2(9)$ = 166.6, P <

324 0.001; neck elevation, $\chi^2(9)$ = 55.9, P < 0.001), tending to accumulate in bins toward the

325 periphery and with lower cumulative occupancy. **(B)** The distributions of tuning peaks in M2

326 were also non-uniform, tending to accrete in peripheral bins with lower occupancy (top to

327 bottom: head pitch, $\chi^2(9)$ = 123, P <0.001; head azimuth, $\chi^2(9)$ = 51.5, P < 0.001; head roll,

328 $\chi^2(9)$ = 38.4, P < 0.001; back pitch, $\chi^2(9)$ = 106, P < 0.001; back azimuth, $\chi^2(9)$ = 123.5, P < 0.001;

329 neck elevation, $\chi^2(9)$ = 63.9, P < 0.001). **(C)** (Left) Cumulative occupancy for all egocentric

330 positions sampled across animals; (right) same data, but on a log scale to show that all bins

331 had ≥5 sec of sampling.

332

333

334

335

336

337

338

339

340

341

342

343

A

PPC

Light

Dark

Light

Firing rate (Hz)

Head Azimuth (°)   Back Pitch (°)   Neck Elevation (cm)

B

All Head Stability   All Back Stability   Neck Stability

n = 139   n = 79   n = 39
n.s.   n.s.   n.s.

cumulative %

Correlation

○ light – light'
● light – dark

C

M2

Light

Dark

Light

Firing rate (Hz)

Head Azimuth (°)   Back Pitch (°)   Neck Elevation (cm)

D

All Head Stability   All Back Stability   Neck Stability

n = 136   n = 70   n = 43
D = 0.17   n.s.   n.s.
P<0.05

cumulative %

Correlation

○ light – light'
● light – dark
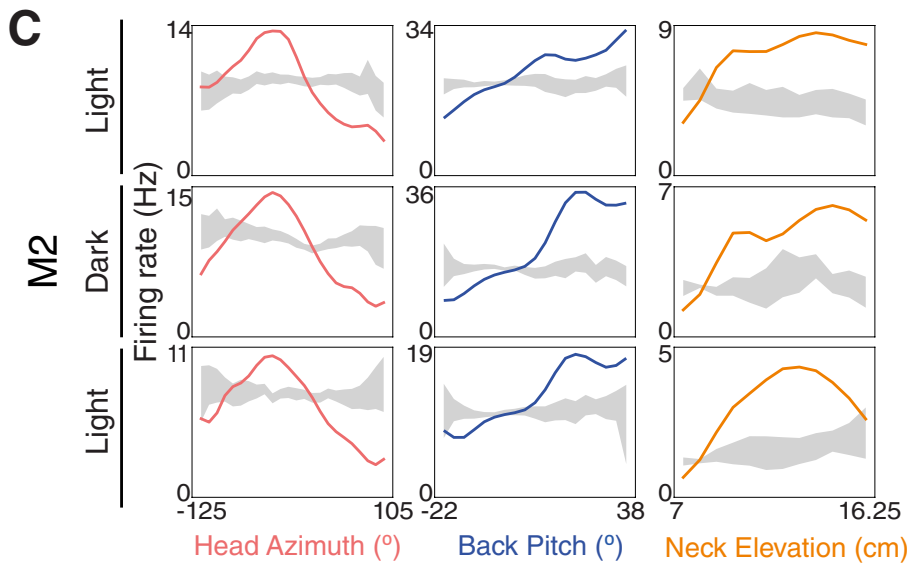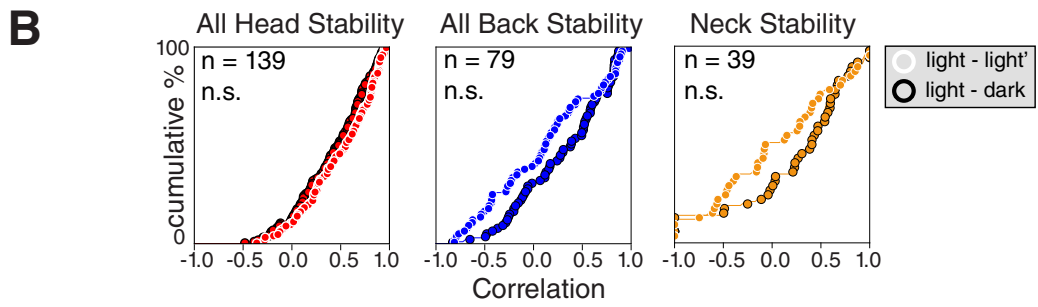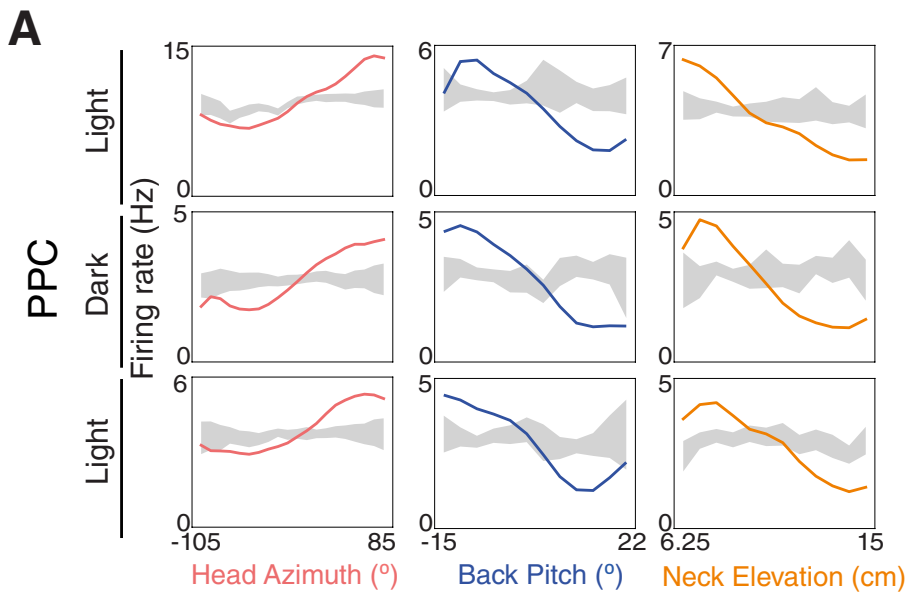
344   **Fig. S4. Postural tuning in PPC and M2 was stable across light and dark sessions**

345   **(A**) Examples of three cells in PPC with stable tuning to head azimuth (left), back pitch (middle)

346   and neck elevation (right) in light and dark sessions. **(B)** Cumulative frequency distributions of

347   Pearson's correlations for all features of the head (left), back (middle) and for neck elevation

348   (right) between two sessions in light, or one light and one dark session. The distributions of

349   correlations did not differ significantly for any comparison (inset, K-S test, $p > 0.05$ in all cases).

350   **(C)** Examples of three M2 cells with stable tuning across light and dark recording sessions

351   (same as **(A)**). **(D)** Cumulative frequency distributions of Pearson's correlations between light-

352   light' and light-dark recording sessions for all head (left) and back features (middle), and neck

353   elevation (right). The stability of tuning curves for the head were the only that varied between

354   light and dark sessions, with the light-dark session showing slightly greater stability than the

355   light-light' session ($D = 0.21$, $P < 0.001$).

356

357

358

359

360

361

362

363

364

365

366

367

368

PPC

Cell 1

i = 0.11   3Hz | i = 0.40   6Hz | i = 0.75   8Hz | i = 0.09   1.8Hz | i = 0.15   3Hz | i = 0.12   2Hz | i = 0.11   3Hz

Cell 2

i = 0.12   0.4Hz | i = 0.85   2Hz | i = 0.89   2Hz | i = 0.88   3Hz | i = 0.87   3Hz | i = 0.68   3Hz | i = 0.86   2Hz

Self-motion (cm/s) | Head azimuth (°) | Head roll (°) | Head angular velocity (°/s) | Neck elevation (cm) | Head direction (°) | Running speed (cm/s)

M2

Cell 3

i = 0.10   17Hz | i = 0.74   29Hz | i = 0.71   20Hz | i = 0.52   29Hz | i = 0.48   25Hz | i = 0.69   6Hz | i = 0.73   6Hz

Cell 4

i = 0.30   11Hz | i = 0.97   11Hz | i = 0.94   10Hz | i = 0.73   6Hz | i = 0.97   9Hz | i = 0.94   11Hz | i = 0.95   16Hz

Self-motion (cm/s) | Head azimuth (°) | Head roll (°) | Head angular velocity (°/s) | Neck elevation (cm) | Head direction (°) | Running speed (cm/s)
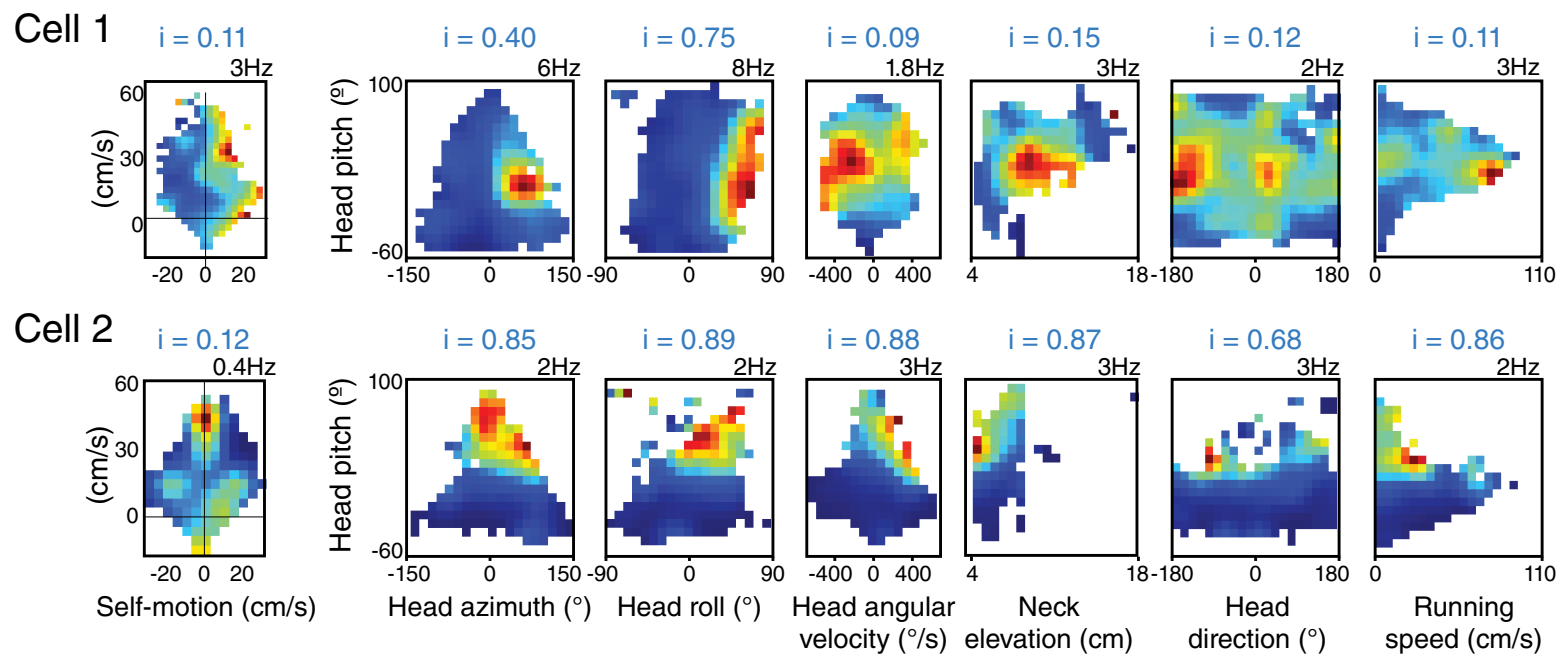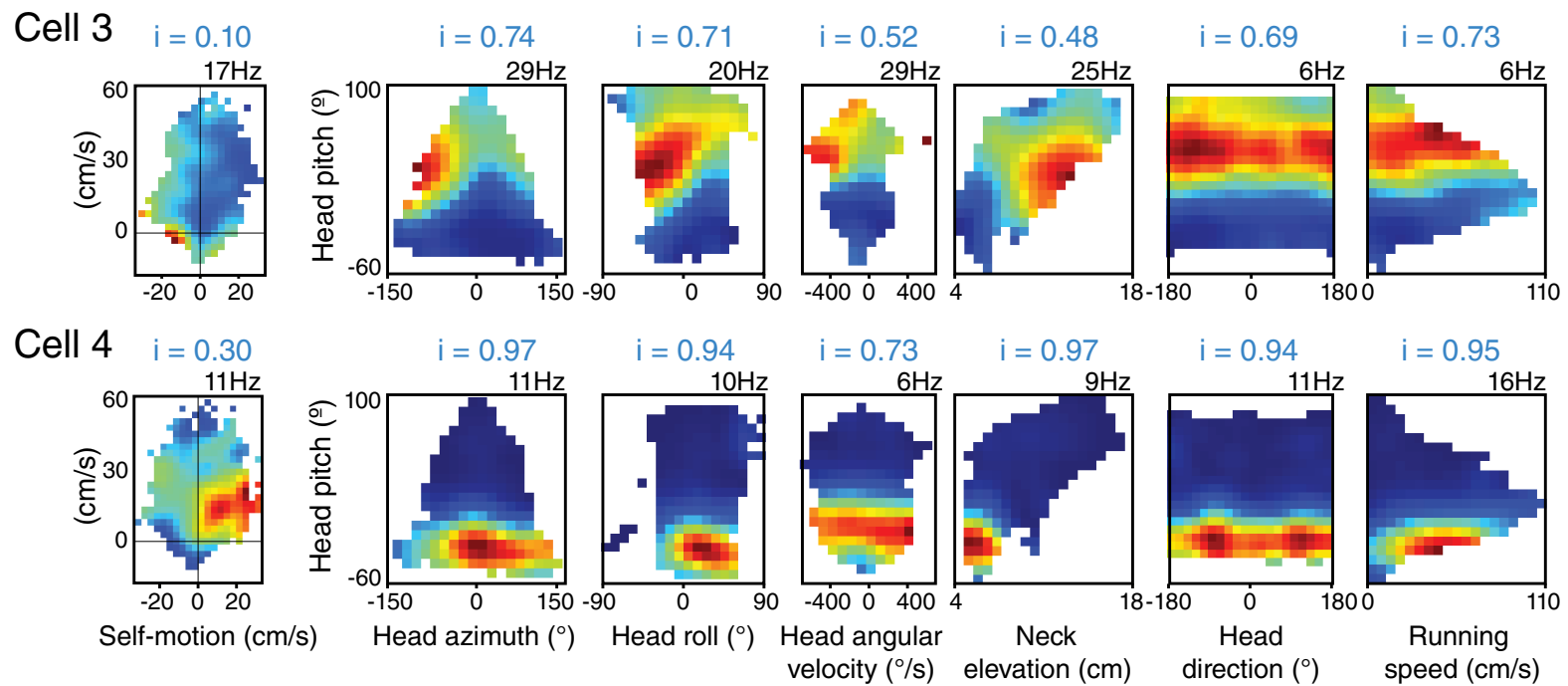
369 **Fig. S5. Examples of postural tuning independent of self-motion in PPC and M2.**

370 Top, Cell 1 in PPC showed little tuning to self-motion (information rate 0.11 bits/sec; blue text

371 above), but had sharp firing fields for combinations of head pitch, azimuth and roll (right, first

372 2 panels). The cell was largely uninformative of angular head velocity, neck elevation, head

373 direction or running speed (reflected by lower information rates). Cell 2 also had poor self-

374 motion tuning, but was highly sensitive to head pitch. Selectivity for head pitch was apparent

375 across interactions, including with angular velocity, neck elevation, head direction and

376 running speed (right panels). Below, Cell 3, from M2, did not have a significant self-motion

377 correlate (information rate =0.10), but was strongly sensitive to combinations of pitch,

378 azimuth and roll of the head (right), and showed little co-modulation by world-referenced

379 features such as head direction or speed. Cell 4 exhibited a self-motion preference for

380 rightward turns (left), but its firing rate was far more informative of head pitch and neck

381 elevation than self-motion. The cell did not distinguish left from right head angular velocities

382 (middle panel), it was not sensitive to head direction, nor was it modulated significantly by

383 running speed. We also note that 3D postural tuning was maintained when self-motion maps

384 were split into leftward or rightward displacements (not shown).
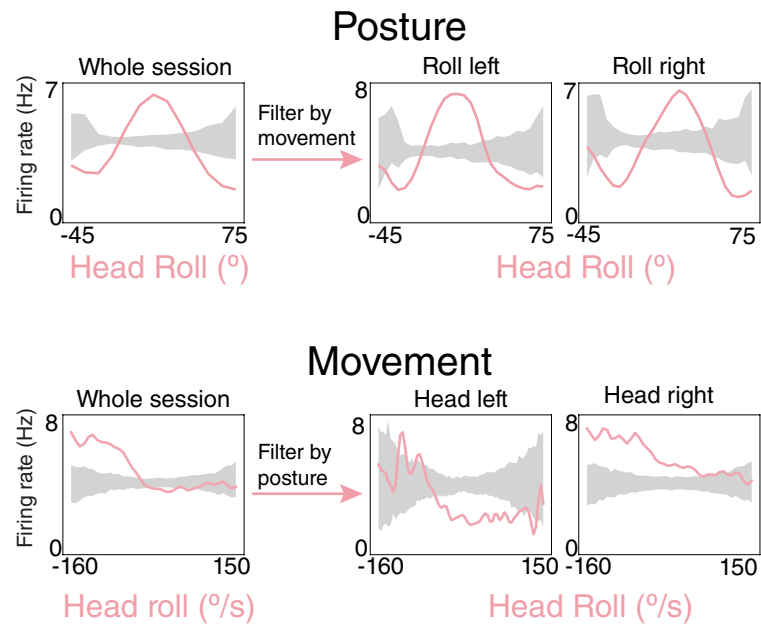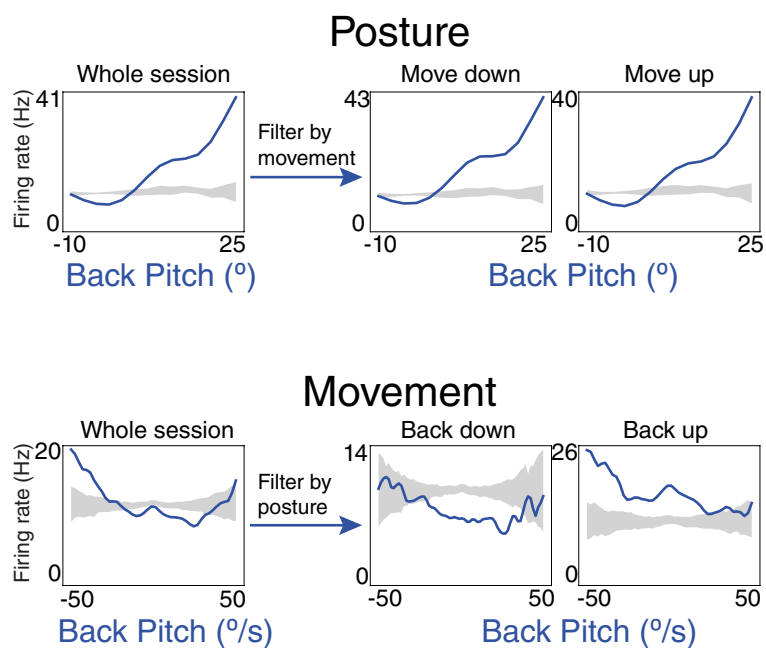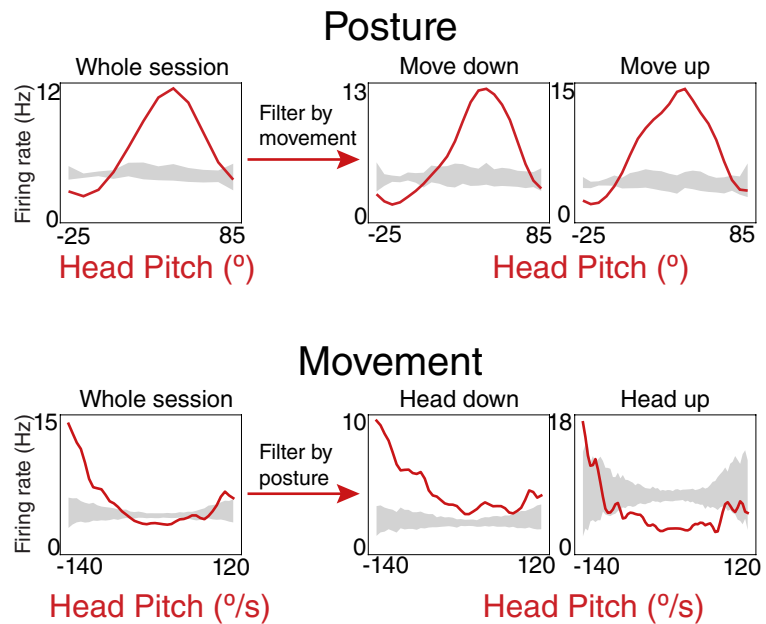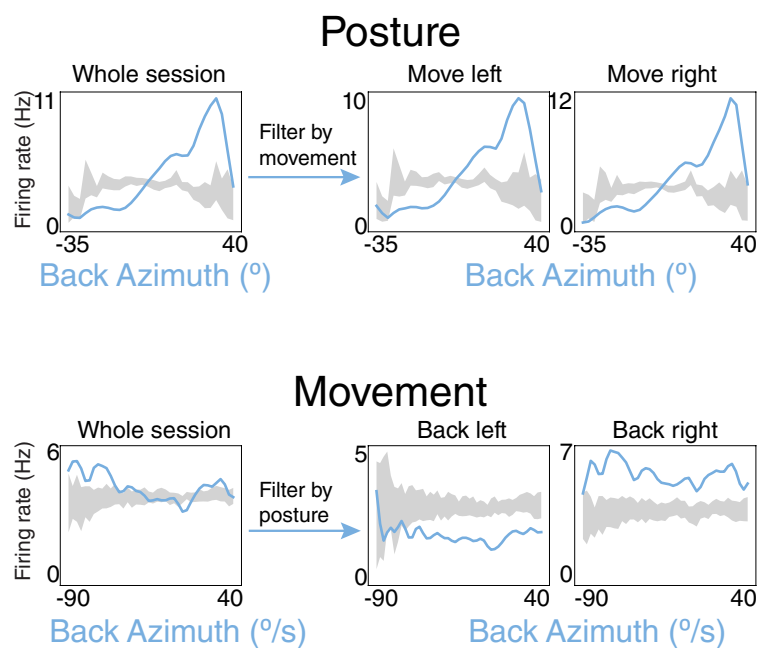
385

386

387

388

389

390

391

392

393

A

PPC cell 1

Posture

Whole session
Firing rate (Hz)
7
Head Roll (º)
-45   75

Filter by movement →

Roll left
8
Head Roll (º)
-45   75

Roll right
7
Head Roll (º)
-45   75

Movement

Whole session
Firing rate (Hz)
8
Head roll (º/s)
-160   150

Filter by posture →

Head left
8
Head Roll (º/s)
-160   150

Head right
8
Head Roll (º/s)
-160   150

PPC cell 2

Posture

Whole session
Firing rate (Hz)
41
Back Pitch (º)
-10   25

Filter by movement →

Move down
43
Back Pitch (º)
-10   25

Move up
40
Back Pitch (º)
-10   25

Movement

Whole session
Firing rate (Hz)
20
Back Pitch (º/s)
-50   50

Filter by posture →

Back down
14
Back Pitch (º/s)
-50   50

Back up
26
Back Pitch (º/s)
-50   50

B

M2 cell 1

Posture

Whole session
Firing rate (Hz)
12
Head Pitch (º)
-25   85

Filter by movement →

Move down
13
Head Pitch (º)
-25   85

Move up
15
Head Pitch (º)
-25   85

Movement

Whole session
Firing rate (Hz)
15
Head Pitch (º/s)
-140   120

Filter by posture →

Head down
10
Head Pitch (º/s)
-140   120

Head up
18
Head Pitch (º/s)
-140   120

M2 cell 2

Posture

Whole session
Firing rate (Hz)
11
Back Azimuth (º)
-35   40

Filter by movement →

Move left
10
Back Azimuth (º)
-35   40

Move right
12
Back Azimuth (º)
-35   40

Movement

Whole session
Firing rate (Hz)
6
Back Azimuth (º/s)
-90   40

Filter by posture →

Back left
5
Back Azimuth (º/s)
-90   40

Back right
7
Back Azimuth (º/s)
-90   40

394   **Fig. S6. Splitting sessions by posture or movement reveals the primacy of posture**.

395   **(A)** (top, left) 1D tuning curve of a PPC neuron (Cell 1) tuned to head roll. (top, right) The

396   recording session was split to only include leftward or rightward angular velocities for head

397   roll, but this had no effect on postural tuning, demonstrating that posture was encoded

398   independently of head movement. Immediately below, the firing rate Cell 1 is expressed as a

399   function of angular head roll velocity, and the session is split (right) for when the head was

400   rolled left or right (i.e position of the head). The velocity tuning curve of Cell 1 was not stable

401   for the different head postures, demonstrating that apparent-velocity tuning in fact

402   depended on the angle of the head. (below, left) The same comparisons were made for

403   another PPC cell (Cell 2) tuned to back pitch, from a different recording session. As with the

404   example above, tuning to pitch was invariant with regard to movement speed, but the

405   apparent tuning to movement (below) varied substantially depending on the angle of the

406   back. **(B)** (top) The same test was performed on an M2 neuron tuned to head pitch, which

407   again demonstrated that postural tuning for the head was independent of movement

408   velocity, but not vice versa. (bottom) An M2 cell showing the same effect for tuning to back
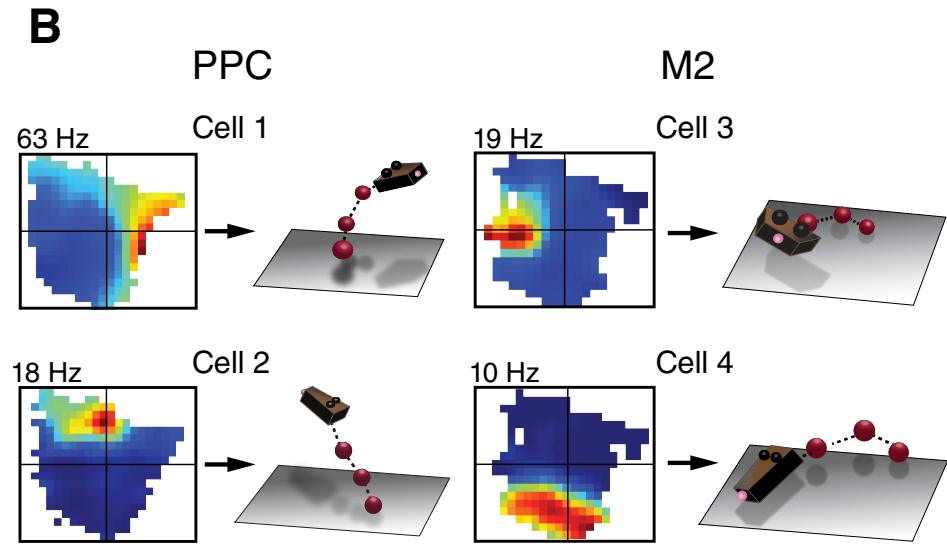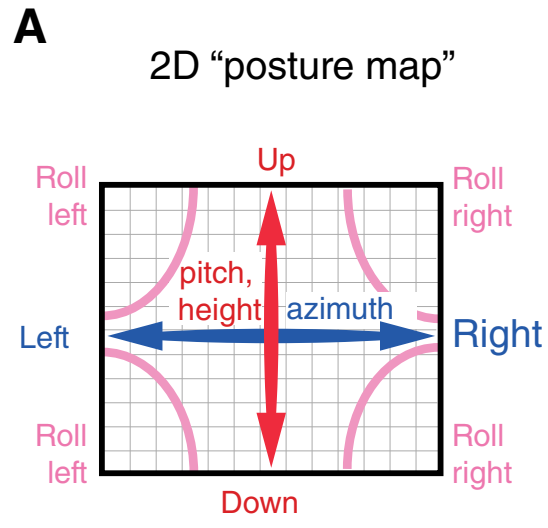
409   azimuth.

410

411

412

413

414

415

416

417

418

A

2D "posture map"

B

PPC   M2

419   **Fig. S7. Dimensionality reduction for visualization of postural tuning with a 2D rate map.**

420   **(A)** The six postural features we measured (head pitch, azimuth and roll, neck elevation, back

421   pitch and azimuth) were rendered onto a single 2D surface using Isomap (Tenenbaum, 2000).

422   Vertical features, such as head pitch, back pitch and neck height, are stretched along the

423   ordinate (red arrow); head and back azimuth are represented along the abscissa (blue arrow);

424   head roll (pink) occupies the corners. **(B)** Two example PPC cells (left) and two M2 cells (right)

425   show discrete firing fields on 2D posture maps corresponding to the 3D postures of the rat

426   models to the right. Population-level activity was used to decode dynamic position on the

427   posture map in Figure 4A and Supplementary videos 7-8.

428

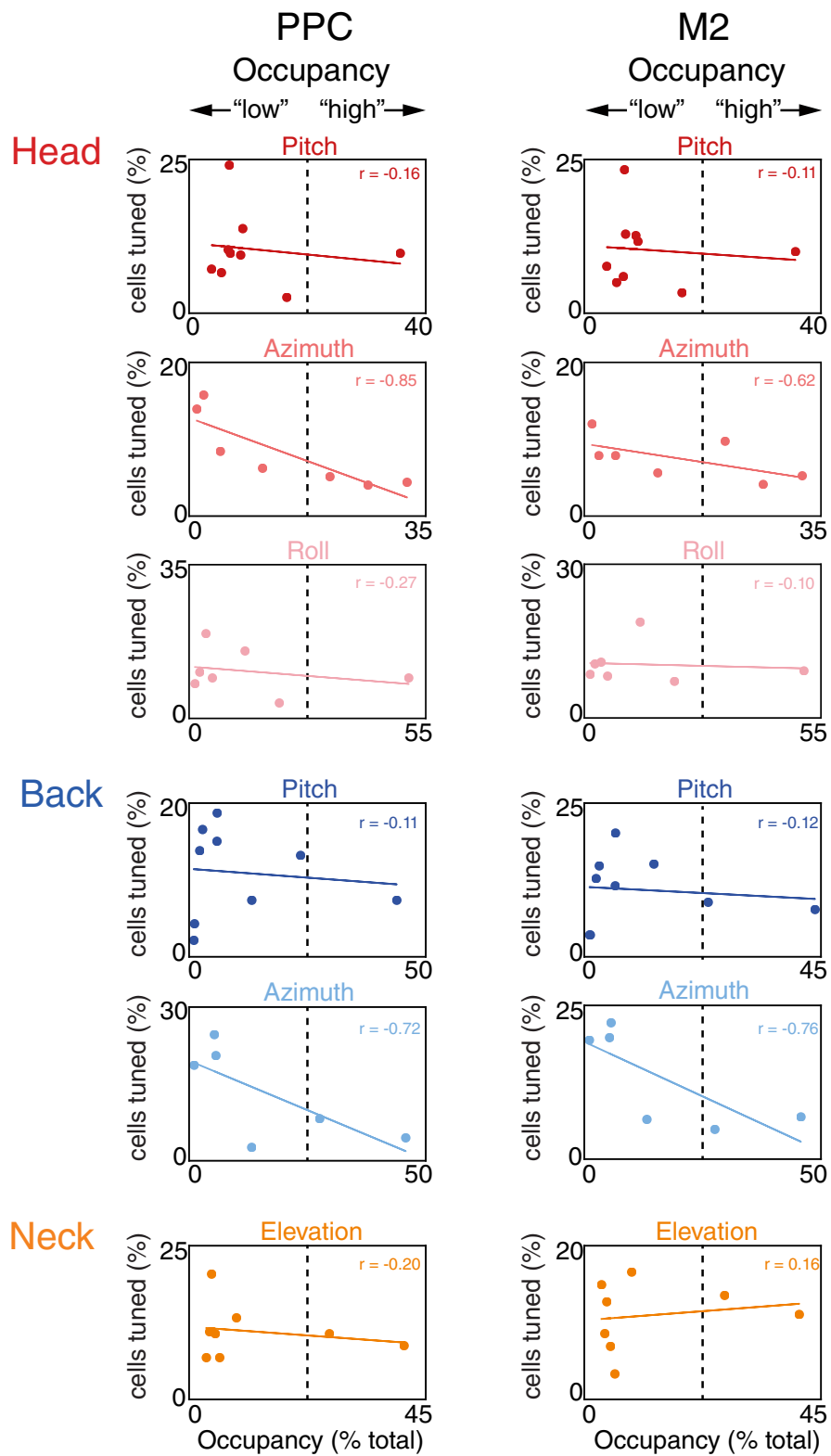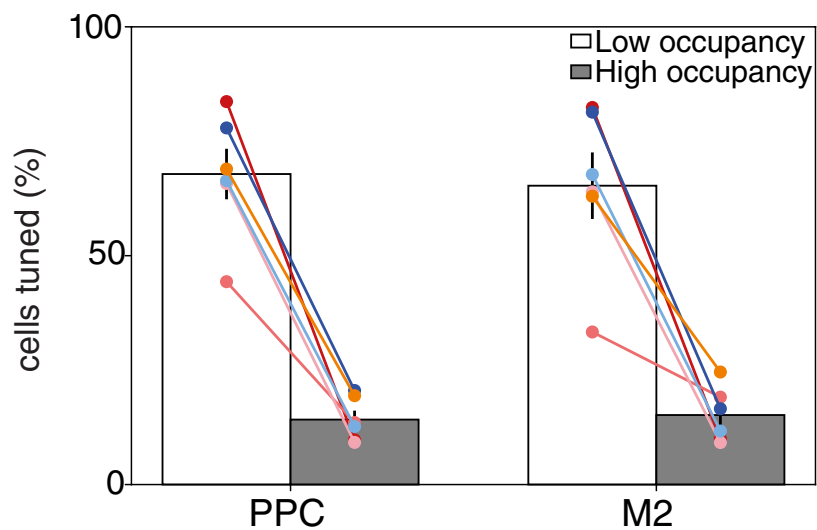429

430

431

432

433

434

435

436

437

438

439

440

441

442

443

444 **Fig. S8. For all features, the majority of cells had tuning peaks at positions with <50%**

445 **occupancy.**

446 **(A)** The duration that each bin was occupied for measures of head, neck and back position (as

447 shown in Fig.4 (A) and (B)) was divided by total recording time to determine the percent

448 occupancy per bin. Bins with <1% occupancy were excluded. The percentage of cells with

449 significant tuning peaks (>3 SD above shuffled) was higher for posture bins with below-mean

450 occupancy (e.g. for head pitch in both PPC and M2, 83% of cells had tuning peaks in bins with

451 less than 20% relative occupancy). The inverse relationship between the number of tuned

452 cells and occupancy was particularly clear for head and back azimuth. **(B)** Summary of results

453 obtained in **(A)**. The percentages of cells tuned were summed across levels of high/low

454 occupancy in both regions, showing that that the mean percentage of cells tuned for "low

455 occupancy" in PPC was 68% (99% CI: 53-82%), while the mean percentage for "high

456 occupancy" was 14% (99% CI: 9-19%). For M2, the mean percentage for low occupancy was

457 65% (99% CI: 47-84%), and 15% (99% CI: 9-22%) for "high occupancy." Bar graphs depict the

458 mean ±SEM.

459

460

461

462

463

464

465

466

467

468

Table S1. Stability of 1D tuning curves

Feature	PPC			M2		
	# cells[1]	# stable cells[2]	% stable[3]	# cells	# stable cells	% stable
Head pitch	296	191	64.5%	341	218	63.9%
Head azimuth	233	128	54.9%	208	117	56.2%
Head roll	191	137	71.7%	236	156	66.1%
Back pitch	277	121	43.6%	269	140	52.0%
Back azimuth	220	113	51.3%	190	87	45.7%
Neck elevation	260	143	55.0%	286	167	58.4%

[1]Number of cells with tuning curve peaks exceeding the 99th percentile of the shuffled distribution in the first recording session. All cells from PPC (n = 729) and M2 (n = 808) were considered for each feature.
[2]Number of cells from the first column with across-session r-value exceeding the 95th percentile of the shuffled data.
[3](Column 2 / column 1) x 100.

Table S2 Summary of GLM model selection for all cells

PPC n = 729

Head — n = 237 (32.5%)

Behavioral feature	Move-ment	Pitch	Azimuth	Roll	Pitch x azimuth	Pitch x roll	Roll x azimuth	Head all	Head all x neck height
Cell count	12	51	25	59	15	22	13	21	19

Neck — n = 43 (5.9%)

Behavioral feature	Move-ment	Neck height
Cell count	7	36

Back — n = 69 (9.5%)

Behavioral feature	Move-ment	Pitch	Azimuth	Pitch x azimuth
Cell count	22	20	17	10

All body

Behavioral feature	All pose variables	Self-motion	Speed	Direction	Position	Unclas-sified
Cell count	29	15	38	5	1	292

M2 n = 808

Head — n = 316 (39.1%)

Behavioral feature	Move-ment	Pitch	Azimuth	Roll	Pitch x azimuth	Pitch x roll	Roll x azimuth	Head all	Head all x neck height
Cell count	11	86	8	47	22	65	7	28	42

Neck — n = 84 (10.4%)

Behavioral feature	Move-ment	Neck height
Cell count	10	74

Back — n = 75 (9.3%)

Behavioral feature	Move-ment	Pitch	Azimuth	Pitch x azimuth
Cell count	8	57	6	4

All body

Behavioral feature	All pose variables	Self-motion	Speed	Direction	Position	Unclas-sified
Cell count	27	4	26	6	11	259

Supplementary movies

Movie S1. Animated demonstration of the behavioral arena and recreated 3D rat as rendered in our graphical user interface (GUI). Rats are portrayed by their head, back (3 red spheres), and neck (smaller green sphere).

Movie S2. Overhead view of a rat foraging in the open field in the GUI. The animal is held in place artificially to visualize movement of the body. Spiking activity of a single PPC neuron can be heard when the animal flexes its head and spine to the right.

Movie S3. Same as Movie S2, though in a different animal and viewed from the side, with a PPC neuron driven by rearing.

Movie S4. Example of an M2 neuron selective for leftward roll of the head.

Movie S5. An M2 neuron driven by the combined turning of the head to the right while the animal is reared up. The neuron continues to spike while the animal remains still in the cell's preferred posture.

Movie S6. A PPC neuron that fires maximally when the head is raised at a high angle relative to the back, tending to occur just before rearing.

Movie S7. (left) 3D animation depicting the behavior of a rat in the open field, played at 1/3 speed. **(right)** Synchronized frame-by-frame decoding of the animal's posture on a 2D "posture map" using simultaneously recorded ensembles in PPC and M2. The true posture of the rat is indicated by a green "X", and color-coding depicts the posterior distribution of the animal's posture estimated using spiking activity from PPC and M2.

Movie S8. Same as Movie S7, taken from later in the same recording session.

References and Notes

1. H. Head, G. Holmes, Sensory disturbances from cerebral lesions I. *Brain* **34**, 102–254 (1911). doi:10.1093/brain/34.2-3.102

2. M. Critchley, *The Parietal Lobes* (Williams and Wilkins, 1953).

3. V. B. Mountcastle, J. C. Lynch, A. Georgopoulos, H. Sakata, C. Acuna, Posterior parietal association cortex of the monkey: Command functions for operations within extrapersonal space. *J. Neurophysiol.* **38**, 871–908 (1975). doi:10.1152/jn.1975.38.4.871 Medline

4. J. Tanji, E. V. Evarts, Anticipatory activity of motor cortex neurons in relation to direction of an intended movement. *J. Neurophysiol.* **39**, 1062–1068 (1976). doi:10.1152/jn.1976.39.5.1062 Medline

5. R. A. Andersen, V. B. Mountcastle, The influence of the angle of gaze upon the excitability of the light-sensitive neurons of the posterior parietal cortex. *J. Neurosci.* **3**, 532–548 (1983). doi:10.1523/JNEUROSCI.03-03-00532.1983 Medline

6. A. P. Georgopoulos, R. E. Kettner, A. B. Schwartz, Primate motor cortex and free arm movements to visual targets in three-dimensional space. II. Coding of the direction of movement by a neuronal population. *J. Neurosci.* **8**, 2928–2937 (1988). doi:10.1523/JNEUROSCI.08-08-02928.1988 Medline

7. J. Wessberg, C. R. Stambaugh, J. D. Kralik, P. D. Beck, M. Laubach, J. K. Chapin, J. Kim, S. J. Biggs, M. A. Srinivasan, M. A. L. Nicolelis, Real-time prediction of hand trajectory by ensembles of cortical neurons in primates. *Nature* **408**, 361–365 (2000). doi:10.1038/35042582 Medline

8. R. A. Andersen, C. A. Buneo, Intentional maps in posterior parietal cortex. *Annu. Rev. Neurosci.* **25**, 189–220 (2002). doi:10.1146/annurev.neuro.25.112701.142922 Medline

9. M. D. Serruya, N. G. Hatsopoulos, L. Paninski, M. R. Fellows, J. P. Donoghue, Instant neural control of a movement signal. *Nature* **416**, 141–142 (2002). doi:10.1038/416141a Medline

10. M. Hauschild, G. H. Mulliken, I. Fineman, G. E. Loeb, R. A. Andersen, Cognitive signals for brain-machine interfaces in posterior parietal cortex include continuous 3D trajectory commands. *Proc. Natl. Acad. Sci. U.S.A.* **109**, 17075–17080 (2012). doi:10.1073/pnas.1215092109 Medline

11. B. Kolb, R. J. Sutherland, I. Q. Whishaw, A comparison of the contributions of the frontal and parietal association cortex to spatial localization in rats. *Behav. Neurosci.* **97**, 13–27 (1983). doi:10.1037/0735-7044.97.1.13 Medline

12. J. C. Erlich, M. Bialek, C. D. Brody, A cortical substrate for memory-guided orienting in the rat. *Neuron* **72**, 330–343 (2011). doi:10.1016/j.neuron.2011.07.010 Medline

13. B. L. McNaughton, S. J. Y. Mizumori, C. A. Barnes, B. J. Leonard, M. Marquis, E. J. Green, Cortical representation of motion during unrestrained spatial navigation in the rat. *Cereb. Cortex* **4**, 27–39 (1994). doi:10.1093/cercor/4.1.27 Medline

14. J. R. Whitlock, G. Pfuhl, N. Dagslott, M. B. Moser, E. I. Moser, Functional split between parietal and entorhinal cortices in the rat. *Neuron* **73**, 789–802 (2012). doi:10.1016/j.neuron.2011.12.028 Medline

15. D. A. Nitz, Tracking route progression in the posterior parietal cortex. *Neuron* **49**, 747–756 (2006). doi:10.1016/j.neuron.2006.01.037 Medline

16. C. D. Harvey, P. Coen, D. W. Tank, Choice-specific sequences in parietal cortex during a virtual-navigation decision task. *Nature* **484**, 62–68 (2012). doi:10.1038/nature10918 Medline

17. A. A. Wilber, B. J. Clark, T. C. Forster, M. Tatsuno, B. L. McNaughton, Interaction of egocentric and world-centered reference frames in the rat posterior parietal cortex. *J. Neurosci.* **34**, 5431–5446 (2014). doi:10.1523/JNEUROSCI.0511-14.2014 Medline

18. E. B. Cutrell, R. T. Marrocco, Electrical microstimulation of primate posterior parietal cortex initiates orienting and alerting components of covert attention. *Exp. Brain Res.* **144**, 103–113 (2002). doi:10.1007/s00221-002-1032-x Medline

19. K. Hardcastle, N. Maheswaranathan, S. Ganguli, L. M. Giocomo, A multiplexed, heterogeneous, and adaptive code for navigation in medial entorhinal cortex. *Neuron* **94**, 375–387.e7 (2017). doi:10.1016/j.neuron.2017.03.025 Medline

20. J. Hyvärinen, Regional distribution of functions in parietal association area 7 of the monkey. *Brain Res.* **206**, 287–303 (1981). doi:10.1016/0006-8993(81)90533-3 Medline

21. I. Stepniewska, P. C. Fang, J. H. Kaas, Microstimulation reveals specialized subregions for different complex movements in posterior parietal cortex of prosimian galagos. *Proc. Natl. Acad. Sci. U.S.A.* **102**, 4878–4883 (2005). doi:10.1073/pnas.0501048102 Medline

22. R. D. Hall, E. P. Lindholm, Organization of motor and somatosensory neocortex in albino rat. *Brain Res.* **66**, 23–38 (1974). doi:10.1016/0006-8993(74)90076-6

23. M. Brecht, A. Krauss, S. Muhammad, L. Sinai-Esfahani, S. Bellanca, T. W. Margrie, Organization of rat vibrissa motor cortex and adjacent areas according to cytoarchitectonics, microstimulation, and intracellular stimulation of identified cells. *J. Comp. Neurol.* **479**, 360–373 (2004). doi:10.1002/cne.20306 Medline

24. S. P. Wise, D. Boussaoud, P. B. Johnson, R. Caminiti, Premotor and parietal cortex: Corticocortical connectivity and combinatorial computations. *Annu. Rev. Neurosci.* **20**, 25–42 (1997). doi:10.1146/annurev.neuro.20.1.25 Medline

25. G. Rizzolatti, L. Fogassi, V. Gallese, Parietal cortex: From sight to action. *Curr. Opin. Neurobiol.* **7**, 562–567 (1997). doi:10.1016/S0959-4388(97)80037-2 Medline

26. B. Pesaran, M. J. Nelson, R. A. Andersen, Free choice activates a decision circuit between frontal and parietal cortex. *Nature* **453**, 406–409 (2008). doi:10.1038/nature06849 Medline

27. T. D. Hanks, C. D. Kopec, B. W. Brunton, C. A. Duan, J. C. Erlich, C. D. Brody, Distinct relationships of parietal and prefrontal cortices to evidence accumulation. *Nature* **520**, 220–223 (2015). doi:10.1038/nature14066 Medline

28. J. B. Tenenbaum, V. de Silva, J. C. Langford, A global geometric framework for nonlinear dimensionality reduction. *Science* **290**, 2319–2323 (2000). doi:10.1126/science.290.5500.2319 Medline

29. P. R. Brotchie, R. A. Andersen, L. H. Snyder, S. J. Goodman, Head position signals used by parietal neurons to encode locations of visual stimuli. *Nature* **375**, 232–235 (1995). doi:10.1038/375232a0 Medline

30. A. P. Batista, C. A. Buneo, L. H. Snyder, R. A. Andersen, Reach plans in eye-centered coordinates. *Science* **285**, 257–260 (1999). doi:10.1126/science.285.5425.257 Medline

31. E. Salinas, P. Thier, Gain modulation: A major computational principle of the central nervous system. *Neuron* **27**, 15–21 (2000). doi:10.1016/S0896-6273(00)00004-0 Medline

32. G. H. Mulliken, S. Musallam, R. A. Andersen, Decoding trajectories from posterior parietal cortex ensembles. *J. Neurosci.* **28**, 12913–12926 (2008). doi:10.1523/JNEUROSCI.1463-08.2008 Medline

33. L. Fogassi, V. Gallese, L. Fadiga, G. Luppino, M. Matelli, G. Rizzolatti, Coding of peripersonal space in inferior premotor cortex (area F4). *J. Neurophysiol.* **76**, 141–157 (1996). doi:10.1152/jn.1996.76.1.141 Medline

34. T. M. Pearce, D. W. Moran, Strategy-dependent encoding of planned arm movements in the dorsal premotor cortex. *Science* **337**, 984–988 (2012). doi:10.1126/science.1220642 Medline

35. G. M. Shepherd, Corticostriatal connectivity and its role in disease. *Nat. Rev. Neurosci.* **14**, 278–291 (2013). doi:10.1038/nrn3469 Medline

36. G. Cui, S. B. Jun, X. Jin, M. D. Pham, S. S. Vogel, D. M. Lovinger, R. M. Costa, Concurrent activation of striatal direct and indirect pathways during action initiation. *Nature* **494**, 238–242 (2013). doi:10.1038/nature11846 Medline

37. J. J. Wilson, N. Alexandre, C. Trentin, M. Tripodi, Three-dimensional representation of motor space in the mouse superior colliculus. *Curr. Biol.* **28**, 1744–1755.e12 (2018). doi:10.1016/j.cub.2018.04.021 Medline

38. M. S. Esposito, P. Capelli, S. Arber, Brainstem nucleus MdV mediates skilled forelimb motor tasks. *Nature* **508**, 351–356 (2014). doi:10.1038/nature13023 Medline

39. J. E. Markowitz, W. F. Gillis, C. C. Beron, S. Q. Neufeld, K. Robertson, N. D. Bhagat, R. E. Peterson, E. Peterson, M. Hyun, S. W. Linderman, B. L. Sabatini, S. R. Datta, The striatum organizes 3D behavior via moment-to-moment action selection. *Cell* **174**, 44–58.e17 (2018). doi:10.1016/j.cell.2018.04.019

40. X. Chen, G. C. Deangelis, D. E. Angelaki, Diverse spatial reference frames of vestibular signals in parietal cortex. *Neuron* **80**, 1310–1321 (2013). doi:10.1016/j.neuron.2013.09.006 Medline

41. F. Klam, W. Graf, Vestibular response kinematics in posterior parietal cortex neurons of macaque monkeys. *Eur. J. Neurosci.* **18**, 995–1010 (2003). doi:10.1046/j.1460-9568.2003.02813.x Medline

42. N. S. Harper, D. McAlpine, Optimal neural population coding of an auditory spatial cue. *Nature* **430**, 682–686 (2004). doi:10.1038/nature02768 Medline

43. D. Ganguli, E. P. Simoncelli, Efficient sensory encoding and Bayesian inference with heterogeneous neural populations. *Neural Comput.* **26**, 2103–2134 (2014). doi:10.1162/NECO_a_00638 Medline

44. B. Mimica, Efficient cortical coding of 3D posture in freely behaving rats – data and GUI, Norstore (2018); https://doi.org/10.11582/2018.00028.

45. M. Fyhn, S. Molden, M. P. Witter, E. I. Moser, M.-B. Moser, Spatial representation in the entorhinal cortex. *Science* **305**, 1258–1264 (2004). doi:10.1126/science.1099901

46. M. Pachitariu, N. Steinmetz, S. Kadir, M. Carandini, K. D. Harris, Kilosort: Realtime spike-sorting for extracellular electrophysiology with hundreds of channels. bioRxiv 061481 [Preprint]. 30 June 2016. https://doi.org/10.1101/061481.

47. K. S. Arun, T. S. Huang, S. D. Blostein, Least-squares fitting of two 3-D point sets. *IEEE Trans. Pattern Anal. Machine Intell.* **9**, 698–700 (1987). doi:10.1109/TPAMI.1987.4767965 Medline

48. J. A. Nelder, W. M. Wedderburn, Generalized linear models. *J. R. Stat. Soc. Ser. A* **135**, 370–384 (1972). doi:10.2307/2344614

49. F. Pedregosa, G. Varoquaux, A. Gramfort, V. Michel, B. Thirion, O. Grisel, M. Blondel, P. Prettenhofer, R. Weiss, V. Dubourg, J. Vanderplas, A. Passos, D. Cournapeau, M. Brucher, M. Perrot, É. Duchesnay, Scikit-learn: Machine learning in Python. *J. Mach. Learn. Res.* **12**, 2825–2830 (2011).

50. D. G. Krige, A statistical approach to some basic mine valuation problems on the Witwatersrand. *J. Chem. Metall. Min. Soc. S. Afr.* **52**, 119–139 (1951).

51. G. Paxinos, C. Watson, *The Rat Brain in Stereotaxic Coordinates* (Academic Press, 2013).